Fast implementation of FEM for integral fractional Laplacian on rectangular meshes

Changtao Sheng[1], Li-Lian Wang[2,*], Hongbin Chen[3], and Huiyuan Li[4]

[1] *School of Mathematics, Shanghai University of Finance and Economics, Shanghai 200433, China.*
[2] *Division of Mathematical Sciences, School of Physical and Mathematical Sciences, Nanyang Technological University, 637371, Singapore.*
[3] *Institute of Mathematics and Physics, College of Science, Central South University of Forestry and Technology, Changsha, Hunan, 410004, China.*
[4] *State Key Laboratory of Computer Science/Laboratory of Parallel Computing, Institute of Software, Chinese Academy of Sciences, Beijing 100190, China.*

Abstract. We show that the entries of the stiffness matrix, associated with the C^0-piecewise linear finite element discretization of the hyper-singular integral fractional Laplacian (IFL) on rectangular meshes, can be simply expressed as one-dimensional integrals on a finite interval. Particularly, the FEM stiffness matrix on uniform meshes has a block-Toeplitz structure, so the matrix-vector multiplication can be implemented by FFT efficiently. The analytic integral representations not only allow for accurate evaluation of the entries, but also facilitate the study of some intrinsic properties of the stiffness matrix. For instance, we can obtain the asymptotic decay rate of the entries, so the "dense" stiffness matrix turns out to be "sparse" with an $O(h^3)$ cutoff. We provide ample numerical examples of PDEs involving the IFL on rectangular or L-shaped domains to demonstrate the optimal convergence and efficiency of this semi-analytical approach. With this, we can also offer some benchmarks for the FEM on general meshes implemented by other means (e.g., for accuracy check and comparison when triangulation reduces to rectangular meshes).

AMS subject classifications: 15B05, 41A05, 41A25, 74S05

Key words: Integral fractional Laplacian, nonlocal/singular operators, FEM on rectangular meshes, stiffness matrix with Toeplitz structure.

1 Introduction

There has been a fast growing interest in nonlocal models in terms of numerics, analysis and applications, which can be testified by the recent review articles [8,20,31] and mono-

*Corresponding author. *Email addresses:* ctsheng@sufe.edu.cn (C. Sheng), lilian@ntu.edu.sg (L.-L. Wang), hongbinchen@csuft.edu.cn (H. Chen), huiyuan@iscas.ac.cn (H. Li)

graphs [19,21], together with many references therein. Among several types of nonlocal operators, the integral fractional Laplacian (IFL) is deemed as one of the most prominent, but challenging operators to deal with. It is known that given a sufficiently nice function $u(\boldsymbol{x})\colon\mathbb{R}^d\to\mathbb{R}$ and $s\in(0,1)$, its IFL $(-\Delta)^s u(\boldsymbol{x})$ has the hypersingular integral representation (cf. [35]):

$$(-\Delta)^s u(\boldsymbol{x}) = C_{d,s}\,\text{p.v.}\int_{\mathbb{R}^d}\frac{u(\boldsymbol{x})-u(\boldsymbol{y})}{|\boldsymbol{x}-\boldsymbol{y}|^{d+2s}}\,\mathrm{d}\boldsymbol{y},\quad C_{d,s}:=\frac{2^{2s}s\Gamma(s+d/2)}{\pi^{d/2}\Gamma(1-s)},\tag{1.1}$$

where "p.v." stands for the principal value and $C_{d,s}$ is the normalisation constant. It can also be defined as a pseudo-differential operator with symbol $|\boldsymbol{\xi}|^{2s}$ through the Fourier transform:

$$(-\Delta)^s u(\boldsymbol{x}) = \mathscr{F}^{-1}\big[|\boldsymbol{\xi}|^{2s}\mathscr{F}[u](\boldsymbol{\xi})\big](\boldsymbol{x}),\quad \boldsymbol{x}\in\mathbb{R}^d.\tag{1.2}$$

The nonlocal and singular nature of this operator poses major difficulties in discretisation and analysis.

Most recent concerns are with PDEs involving the IFL operator on an open bounded Lipschitz domain $\Omega\subset\mathbb{R}^d$. More precisely, given $f:\Omega\to\mathbb{R}$ in a suitable space, we look for u on Ω satisfying the fractional Poisson equation with the (nonlocal) homogeneous Dirichlet boundary condition:

$$(-\Delta)^s u(\boldsymbol{x}) = f(\boldsymbol{x})\quad\text{in}\,\Omega;\quad u(\boldsymbol{x})=0\quad\text{on}\,\Omega^c:=\mathbb{R}^d\backslash\Omega.\tag{1.3}$$

We also intend to apply the FEM solver to spatial discretisation of the fractional diffusion equation:

$$u_t(\boldsymbol{x},t)+(-\Delta)^s u(\boldsymbol{x},t) = F(u(\boldsymbol{x},t))\ \text{in}\,\Omega\times(0,T],\tag{1.4}$$

with the boundary condition: $u=0$ in $\Omega^c\times[0,T]$ and the initial condition: $u|_{t=0}=u_0$ on $\bar{\Omega}$. Here, $F(u)$ is a certain nonlinear functional of u.

1.1 Contributions

In this paper, we provide a semi-analytic means for computing the piecewise linear FEM stiffness matrix for (1.3) and (1.4) on a rectangular domain Ω with a rectangular partition, or a more general domain that can be decomposed into occluded rectangular meshes, e.g., an L-shaped domain. More specifically, given a uniform partition (with mesh size h_x,h_y along x,y, respectively) of Ω with the C^0-piecewise linear tensorial FEM nodal basis: $\{\Phi_{mn}(\boldsymbol{x})=\phi_m(x)\phi_n(y)\}_{1\le m\le M}^{1\le n\le N}$, the fractional stiffness matrix $\boldsymbol{S}=(S_{ll'})$ of size M^2N^2 is a block-Toeplitz matrix that can be generated by an $M\times N$ matrix $\boldsymbol{G}=(G_{kj})$ and each G_{kj} can be explicitly represented as an one-dimensional integral on $(0,\pi/2)$. Such an analytic representation is derived from (i) implementation of FEM in the Fourier transformed domain, and (ii) evaluation of the integral in $\mathbb{R}^2$ using polar coordinates, and judicious use of some analytic formulas in e.g., the handbook [26]. In a nutshell, the main finding is

$$
\begin{aligned}
S_{ll'} &= \big((-\Delta)^{s/2}\Phi_{mn}, (-\Delta)^{s/2}\Phi_{m'n'}\big)_{\mathbb{R}^2} = \int_{\mathbb{R}^2} |\boldsymbol{\xi}|^{2s} \mathscr{F}[\Phi_{mn}](\boldsymbol{\xi}) \overline{\mathscr{F}[\Phi_{m'n'}](\boldsymbol{\xi})} \mathrm{d}\boldsymbol{\xi} \\
&= G_{kj} = \int_0^{\frac{\pi}{2}} g_j^k(\theta)\mathrm{d}\theta, \quad j=|m-m'|, k=|n-n'|, 1\le m\le M, 1\le n\le N,
\end{aligned}
\tag{1.5}
$$

with the index mapping: $l=(n-1)M+m$ and $l'=(n'-1)M+m'$, where the integrand $g_j^k(\theta)$ has removable endpoint singularities and some explicitly known interior singular points. In particular, if $h_x=h_y$, then $G_{kj}=G_{jk}$. As a result, the computation of the entries boils down to evaluating one-dimensional integrals which can be carried out in parallel for each index. We then introduce an efficient and accurate numerical integration technique based upon two essential components: (i) binomial expansions with recursive formulas to remove the endpoint singularities, and (ii) Jacobi-Gauss quadrature with suitable weight functions to absorb interior singularities of $g_j^k(\theta)$. It is worthwhile to point out that the error of the full algorithm is controllable. Benefited from the block-Toeplitz structure of the stiffness matrix, we can avoid computing and saving the MN-by-MN matrix $\boldsymbol{S}$, but the M-by-N generating matrix $\boldsymbol{G}$ instead. In practice, the fast Fourier transform can be applied to solve the structured linear system (cf. [17]).

Needless to say, we oftentimes see the FEM on complex domains with unstructured meshes. For the IFL operator, one can resort to Acosta, Bersetche and Borthagaray [3], and Ainsworth and Glusa [5, 6], which were implemented based on the hypersingular integral representation (1.1). Here, we consider the simple FEM setting (like the finite differences in terms of simple domains, see Duo, Van Wyk and Zhang [22], Duo and Zhang [24], Minden and Ying [34], and Hao, Zhang and Du [28]). Nevertheless, we wish to provide benchmarks for testing general FEM solvers through this simplification, and to study some intrinsic properties of the stiffness matrix (see, for example, Liu et al [32] on the diagonal-dominance of 1D FEM stiffness matrix). Here we find that the entry of $\boldsymbol{G}$ decays like

$$
|G_{kj}| = O\big((j^2+k^2)^{-(s+1)}\big), \quad s\in(0,1), \tag{1.6}
$$

(see Proposition 3.4). This implies that many entries with large j,k can be set to 0, for a given error tolerance (e.g., $O(h^3)$). In this sense, the matrix $\boldsymbol{S}$ is "sparse" (see Fig. 4).

We remark that the setting and idea can be extended to three dimensions using the spherical coordinates for the integral in $\boldsymbol{\xi}\in\mathbb{R}^3$. Accordingly, the integrals in (1.5) will be over a two-dimensional box $[0,\pi/2]^2$ with a much more complicated integrand. Moreover, our approach can be extended to the nonuniform mesh in multi-dimensions but much more complicated and without Toeplitz structure, as with [18] in one-dimensional case.

1.2 Related works

The FEM counts with a solid and well-established theoretical foundation, so it is also preferable for fractional PDEs, after all the IFL operator has interwoven connections with the fractional Sobolev framework (cf. [35]). There have been many recent works devoted to the FEM analysis for fractional PDEs (see, e.g., [4, 10–12, 25]), but the literature on FEM implementation in multiple dimensions is very limited, where it is accomplished based on either the hypersingular integral representation (1.1) [3, 5, 6] or the alternative Dunford-Taylor formulation of the IFL operator [9]. Let $\{\varphi_i\}$ be a set of nodal basis functions associated to a triangulation $\mathcal{T}$ of Ω that vanishes in Ω^c. The fractional stiffness matrix requires to compute

$$\begin{aligned} a_s(\varphi_i,\varphi_j) = &\frac{C_{d,s}}{2}\int_\Omega\int_\Omega \frac{(\varphi_i(\boldsymbol{x})-\varphi_i(\boldsymbol{y}))(\varphi_j(\boldsymbol{x})-\varphi_j(\boldsymbol{y}))}{|\boldsymbol{x}-\boldsymbol{y}|^{d+2s}}\mathrm{d}\boldsymbol{x}\mathrm{d}\boldsymbol{y} \\ &+C_{d,s}\int_\Omega \varphi_i(\boldsymbol{x})\varphi_j(\boldsymbol{x})\left(\int_{\Omega^c}\frac{1}{|\boldsymbol{x}-\boldsymbol{y}|^{d+2s}}\mathrm{d}\boldsymbol{y}\right)\mathrm{d}\boldsymbol{x}, \end{aligned} \tag{1.7}$$

where the former is related to the *regional fractional Laplacian* and the latter counts the external contribution. First, at the element level, one needs to compute the $2d$-integral like

$$\int_T\int_{\widetilde{T}} \frac{(\varphi_i(\boldsymbol{x})-\varphi_i(\boldsymbol{y}))(\varphi_j(\boldsymbol{x})-\varphi_j(\boldsymbol{y}))}{|\boldsymbol{x}-\boldsymbol{y}|^{d+2s}}\mathrm{d}\boldsymbol{x}\mathrm{d}\boldsymbol{y} \tag{1.8}$$

for every pair $T,\widetilde{T}\in\mathcal{T}$ (so the stiffness matrix is dense). If $T\cap\widetilde{T}\neq\emptyset$ (touching element pair), *some sufficiently high order quadrature techniques* must be devised to evaluate such hyper-singular integrals [6]. Second, to deal with the external part, Acosta et al. [3] proposed to surround Ω by a suitable ball B and append an auxiliary mesh $\mathcal{T}_{B\setminus\Omega}$, where the real computation was based on (1.7) with B (resp. B^c) in place of Ω (resp. Ω^c), i.e., on the mesh $\mathcal{T}\cup\mathcal{T}_{B\setminus\Omega}$, and where over 99% of the CPU time was devoted to assembly routine. Ainsworth and Glusa [6] reformulated the second term in (1.7) as a boundary integral form

$$\frac{C_{d,s}}{2s}\int_\Omega \varphi_i(\boldsymbol{x})\varphi_j(\boldsymbol{x})\Big(\int_{\partial\Omega}\frac{\boldsymbol{n}_{\boldsymbol{y}}\cdot(\boldsymbol{x}-\boldsymbol{y})}{|\boldsymbol{x}-\boldsymbol{y}|^{d+2s}}\mathrm{d}\boldsymbol{y}\Big)\mathrm{d}\boldsymbol{x}, \tag{1.9}$$

so that techniques for the boundary element method could be used for the troublesome external part. We remark that Bonito et al. [9] developed the FEM based on the Dunford-Taylor integral form of the IFL, where the sinc quadrature was used in the extra dimension, and a sequence of d-dimensional elliptic problems with quadrature node as parameters in $\mathbb{R}^d$ had to be solved. The aforementioned FEM approaches are amenable to a general domain, but by no means simple.

The finite difference method for IFL can be implemented more tangibly than the FEM, but it is available for simple domains and has a stronger regularity requirement for the solution. We refer to [22–24, 28, 34] for more details. It is noteworthy that Antil et al. [7] introduced a sinc spectral method for the fractional Laplacian in a hypercube where the

Fourier transform of sinc function has a simple explicit representation so the proposed approach can be implemented efficiently in the frequency domain.

The rest of this paper is organized as follows. In section 2, we derive the analytical one-dimensional integral for the entry of the stiffness matrix. In section 3, we describe the detailed algorithm for computing the resulting integrals. In section 4, we provide ample numerical results to show the efficiency and accuracy. We conclude the paper with some discussions on the extension to three dimensions in the last section.

2 Q1-FEM for fractional Laplacian on rectangular meshes

2.1 FEM setting

We consider the piecewise linear finite element approximation of (1.3) on $\Omega \subseteq \mathbb{R}^2$, which can be partitioned by a non-overlapping rectangular mesh (e.g., a rectangle or an L-shaped domain). To fix the idea, we first restrict the discussions to the rectangular domain $\Omega = (a,b) \times (c,d)$ with a partition:

$$\mathcal{T}_h = \big\{ (a+mh_x, c+nh_y) : 0 \le m \le M+1, 0 \le n \le N+1 \big\}, \tag{2.1}$$

where $h_x = \frac{b-a}{M+1}$ and $h_y = \frac{d-c}{N+1}$. Accordingly, we define the approximation space

$$\mathbb{V}_h = \mathrm{span}\big\{ \phi_m(x)\phi_n(y), 1 \le m \le M, 1 \le n \le N \big\}, \tag{2.2}$$

where the piecewise linear FEM basis functions are

$$\phi_\ell(\zeta) = \begin{cases} \frac{\zeta - \zeta_{\ell-1}}{\zeta_\ell - \zeta_{\ell-1}}, & \text{if } \zeta \in (\zeta_{\ell-1}, \zeta_\ell), \\ \frac{\zeta_{\ell+1} - \zeta}{\zeta_{\ell+1} - \zeta_\ell}, & \text{if } \zeta \in (\zeta_\ell, \zeta_{\ell+1}), \\ 0, & \text{elsewhere on } \mathbb{R}, \end{cases} \tag{2.3}$$

for $\zeta_\ell = a + \ell h_x$ or $c + \ell h_y$.

A weak form of (1.3) with $s \in (0,1)$ is to find $u \in \widetilde{H}^s(\Omega) := \{ v \in H^s(\mathbb{R}^2) : v = 0 \text{ in } \Omega^c \}$ such that

$$a_s(u,v) := \big((-\Delta)^{s/2} u, (-\Delta)^{s/2} v \big)_{\mathbb{R}^2} = (f,v)_\Omega, \quad \forall v \in \widetilde{H}^s(\Omega), \tag{2.4}$$

where $(\cdot,\cdot)_{\mathbb{R}^2}$ and $(\cdot,\cdot)_\Omega$ are the inner products on $\mathbb{R}^2$ and Ω, respectively, and $H^s(\mathbb{R}^2)$ denotes the fractional Sobolev space defined by the Fourier transform as usual. Then the FEM for (2.4) is to find $u_h \in \mathbb{V}_h$ such that

$$a_s(u_h,v_h) := \big((-\Delta)^{s/2} u_h, (-\Delta)^{s/2} v_h \big)_{\mathbb{R}^2} = (f,v_h)_\Omega, \quad \forall v_h \in \mathbb{V}_h. \tag{2.5}$$

It is known that both (2.4)-(2.5) are well-posed by the standard Lax-Milgram Lemma.

Given this setting, we intend to explore the best possible analytic information for accurately computating the entries of the stiffness matrix. Write

$$u_h(x,y)=\sum_{n=1}^{N}\sum_{m=1}^{M}\tilde{u}_{mn}\phi_m(x)\phi_n(y), \tag{2.6}$$

and arrange the unknowns in column-major order, that is,

$$\tilde{\boldsymbol{u}}=\big(\underbrace{\tilde{u}_{11},\tilde{u}_{21},\cdots,\tilde{u}_{M1}}_{n=1},\underbrace{\tilde{u}_{12},\tilde{u}_{22},\cdots,\tilde{u}_{M2}}_{n=2},\cdots\cdots,\underbrace{\tilde{u}_{1N},\tilde{u}_{2N},\cdots,\tilde{u}_{MN}}_{n=N}\big)^t\in\mathbb{R}^{MN}, \tag{2.7}$$

where we note the one-to-one correspondence: $\tilde{u}_{mn}=\tilde{\boldsymbol{u}}_l$ with $l=(n-1)M+m$. Correspondingly, the fractional stiffness matrix $\boldsymbol{S}$ is an $MN\times MN$ symmetric matrix with the entries

$$S_{ll'}=S_{l'l}=\big((-\Delta)^{s/2}\phi_m\phi_n,(-\Delta)^{s/2}\phi_{m'}\phi_{n'}\big)_{\mathbb{R}^2},\quad l'=(n'-1)M+m'. \tag{2.8}$$

The computation of $S_{ll'}$ based on the hypersingular integral definition (1.1) in (1.7)-(1.8) is rather complicated. Given the rectangular mesh and tensorial basis, we take a different routine as follows.

(i) The entries of $\boldsymbol{S}$ are evaluated in the Fourier transformed domain

$$S_{ll'}=S_{l'l}=\int_{\mathbb{R}^2}(\xi^2+\eta^2)^s\mathscr{F}[\phi_m(x)\phi_n(y)](\xi,\eta)\overline{\mathscr{F}[\phi_{m'}(x)\phi_{n'}(y)](\xi,\eta)}\,\mathrm{d}\xi\mathrm{d}\eta. \tag{2.9}$$

The matrix $\boldsymbol{S}$ can be generated by an M-by-N generating matrix $\boldsymbol{G}$, whose entries can be represented as a one-dimensional integral on a finite interval.

(ii) $\boldsymbol{S}$ is a symmetric block-Toeplitz matrix with N^2 blocks, and each block is an M-by-M symmetric Toeplitz matrix. Thus, the matrix-vector multiplication can be carried out by FFT with $O(MN\log MN)$ operations.

2.2 Main result

We first show that the entries of the stiffness matrix can be explicitly represented as one-dimensional integrals as follows.

Theorem 2.1. *For $s\in(0,1)$, the FEM stiffness matrix $\boldsymbol{S}$ is an N-by-N symmetric block-Toeplitz matrix of the form*

$$\boldsymbol{S}=\widehat{C}_s\frac{h_x^{4-2s}}{h_y^2}\begin{bmatrix}\boldsymbol{T}_0 & \boldsymbol{T}_1 & \cdots & \boldsymbol{T}_{N-2} & \boldsymbol{T}_{N-1}\\ \boldsymbol{T}_1 & \boldsymbol{T}_0 & \ddots & \ddots & \boldsymbol{T}_{N-2}\\ \vdots & \ddots & \ddots & \ddots & \vdots\\ \boldsymbol{T}_{N-2} & \ddots & \ddots & \boldsymbol{T}_0 & \boldsymbol{T}_1\\ \boldsymbol{T}_{N-1} & \boldsymbol{T}_{N-2} & \cdots & \boldsymbol{T}_1 & \boldsymbol{T}_0\end{bmatrix}, \tag{2.10}$$

where each block of $\boldsymbol{S}$ is an M-by-M symmetric Toeplitz matrix and the entries are given by

$$\boldsymbol{T}_k=\begin{bmatrix} t_0^k & t_1^k & \cdots & t_{M-2}^k & t_{M-1}^k \\ t_1^k & t_0^k & \ddots & \ddots & t_{M-2}^k \\ \vdots & \ddots & \ddots & \ddots & \vdots \\ t_{M-2}^k & \ddots & \ddots & t_0^k & t_1^k \\ t_{M-1}^k & t_{M-2}^k & \cdots & t_1^k & t_0^k \end{bmatrix}, \quad t_j^k=\int_{-\frac{\pi}{2}}^{\frac{\pi}{2}} f_j^k(\theta)\,\mathrm{d}\theta, \tag{2.11}$$

for $0\le k\le N-1$ *and* $0\le j\le M-1$*, and*

$$f_j^k(\theta)=f_j^k(\theta;s,\varrho)=\frac{1}{\sin^4\theta\cos^4\theta}\sum_{p,q=-2}^{2} c_p c_q\big|(j+p)\cos\theta+(k+q)\varrho\sin\theta\big|^{6-2s}. \tag{2.12}$$

In the above, the constants

$$\widehat{C}_s:=-\frac{1}{4\pi\Gamma(7-2s)\sin(s\pi)},\quad \varrho=\frac{h_y}{h_x},\quad c_{\pm2}=1,\quad c_{\pm1}=-4,\quad c_0=6. \tag{2.13}$$

Proof. Let $\{\phi_\ell\}$ be the FEM basis on uniform grids with grid size h given in (2.3). Then from [32, Lemma 2.1], we have

$$\mathscr{F}_1[\phi_\ell(\zeta)](\chi)=\frac{1}{\sqrt{2\pi}}\int_{\mathbb{R}}\phi_\ell(\zeta)e^{-\mathrm{i}\chi\zeta}\mathrm{d}\zeta=\sqrt{\frac{2}{\pi}}\frac{e^{-\mathrm{i}\zeta_\ell\chi}}{h}\frac{1-\cos(h\chi)}{\chi^2},\quad \forall\chi\in\mathbb{R}, \tag{2.14}$$

where $\mathscr{F}_1$ denotes the one-dimensional Fourier transform in $\mathbb{R}$. Note that in (2.9), the two-dimensional Fourier transform: $\mathscr{F}[\phi_m(x)\phi_n(y)]=\mathscr{F}_1[\phi_m](\xi)\times\mathscr{F}_1[\phi_n](\eta)$ with $h=h_x$ and $h=h_y$, respectively. Thus, we derive from (2.14) and direct calculation that

$$\begin{aligned} S_{ll'}&=\frac{4}{\pi^2h_x^2h_y^2}\int_{\mathbb{R}^2}(\xi^2+\eta^2)^s\left\{e^{\mathrm{i}(m-m')h_x\xi}\frac{(1-\cos(h_x\xi))^2}{\xi^4}\right\}\left\{e^{\mathrm{i}(n-n')h_y\eta}\frac{(1-\cos(h_y\eta))^2}{\eta^4}\right\}\mathrm{d}\xi\,\mathrm{d}\eta\\ &=\frac{16}{\pi^2h_x^2h_y^2}\int_{\mathbb{R}_+^2}(\xi^2+\eta^2)^s\left\{\cos((m-m')h_x\xi)\frac{(1-\cos(h_x\xi))^2}{\xi^4}\right\}\\ &\qquad\cdot\left\{\cos((n-n')h_y\eta)\frac{(1-\cos(h_y\eta))^2}{\eta^4}\right\}\mathrm{d}\xi\,\mathrm{d}\eta\\ &=\frac{16}{\pi^2h_x^2h_y^2}\int_{\mathbb{R}_+^2}(\xi^2+\eta^2)^s\left\{\cos(jh_x\xi)\frac{(1-\cos(h_x\xi))^2}{\xi^4}\right\}\left\{\cos(kh_y\eta)\frac{(1-\cos(h_y\eta))^2}{\eta^4}\right\}\mathrm{d}\xi\,\mathrm{d}\eta, \end{aligned} \tag{2.15}$$

where we denoted $\mathbb{R}_+^2=(0,\infty)^2$, $j=|m-m'|$ and $k=|n-n'|$. This implies the entry $S_{ll'}$ (with $l=(n-1)M+m$ and $l'=(n'-1)M+m'$) only depends on $|m-m'|$ and $|n-n'|$, so $\boldsymbol{S}$ is a block Toeplitz matrix.

In view of the non-separable factor $(\xi^2+\eta^2)^s$ for $s\neq 1$, we resort to the polar coordinate transformation $\xi=\rho\cos\theta$, $\eta=\rho\sin\theta$, and rewrite the above double integral as

$$
\begin{aligned}
S_{ll'} = & \frac{16}{\pi^2 h_x^2 h_y^2}\int_0^{\frac{\pi}{2}}\frac{1}{\cos^4\theta\sin^4\theta}\int_0^\infty \rho^{2s+1}\left\{\cos(jh_x\rho\cos\theta)\frac{(1-\cos(h_x\rho\cos\theta))^2}{\rho^4}\right\} \\
& \cdot\left\{\cos(kh_y\rho\sin\theta)\frac{(1-\cos(h_y\rho\sin\theta))^2}{\rho^4}\right\}\mathrm{d}\rho\,\mathrm{d}\theta = \frac{16}{\pi^2 h_x^2 h_y^2}\int_0^{\frac{\pi}{2}}\frac{g_j^k(\theta)}{\cos^4\theta\sin^4\theta}\mathrm{d}\theta,
\end{aligned}
\tag{2.16}
$$

where we denoted

$$
g_j^k(\theta) := \int_0^\infty \rho^{2s-7}\tilde{f}_j^k(\rho,\theta)\,\mathrm{d}\rho, \tag{2.17}
$$

with

$$
\begin{aligned}
&\tilde{f}_j^k(\rho,\theta) = \cos(a_j\rho)(1-\cos(a_1\rho))^2\cos(b_k\rho)(1-\cos(b_1\rho))^2, \\
&a_j := a_j(\theta) = jh_x\cos\theta, \quad b_k := b_k(\theta) = kh_y\sin\theta.
\end{aligned}
$$

Using the fundamental trigonometric identities, we find

$$
\cos(a_j\rho)(1-\cos(a_1\rho))^2 = \cos(a_j\rho)\Big(\frac{3}{2}-2\cos(a_1\rho)+\frac{1}{2}\cos(2a_1\rho)\Big) = \frac{1}{4}\sum_{p=-2}^{2} c_p\cos(a_{j+p}\rho),
$$

and

$$
\begin{aligned}
\tilde{f}_j^k(\rho,\theta) &= \frac{1}{16}\Big(\sum_{p=-2}^{2} c_p\cos(a_{j+p}\rho)\Big)\Big(\sum_{q=-2}^{2} c_q\cos(b_{k+q}\rho)\Big) \\
&= \frac{1}{16}\sum_{p,q=-2}^{2} c_p c_q\cos(a_{j+p}\rho)\cos(b_{k+q}\rho) \\
&= \frac{1}{32}\sum_{p,q=-2}^{2} c_p c_q\big(\cos((a_{j+p}+b_{k+q})\rho)+\cos((a_{j+p}-b_{k+q})\rho)\big) \\
&= \frac{1}{32}\sum_{p,q=-2}^{2} c_p c_q\big(\cos(\alpha_{pq}\rho)+\cos(\beta_{pq}\rho)\big),
\end{aligned}
$$

where

$$
\begin{aligned}
\alpha_{pq} &:= |a_{j+p}+b_{k+q}| = |(j+p)h_x\cos\theta+(k+q)h_y\sin\theta|, \\
\beta_{pq} &:= |a_{j+p}-b_{k+q}| = |(j+p)h_x\cos\theta-(k+q)h_y\sin\theta|.
\end{aligned}
\tag{2.18}
$$

It is evident that the n-th partial derivative is

$$
\partial_\rho^n\tilde{f}_j^k(\rho,\theta) = \frac{1}{32}\sum_{p,q=-2}^{2} c_p c_q\Big\{(\alpha_{pq})^n\cos\Big(\alpha_{pq}\rho+\frac{n\pi}{2}\Big)+(\beta_{pq})^n\cos\Big(\beta_{pq}\rho+\frac{n\pi}{2}\Big)\Big\}. \tag{2.19}
$$

We proceed with the calculation by using integration by parts. For clarity, we consider two cases: $s\in[\frac{1}{2},1)$ and $(0,\frac{1}{2})$, separately.

(i) $s\in[\frac{1}{2},1)$**:** We derive from (2.17) and integration by parts that

$$\begin{aligned}
g_j^k(\theta) &= \int_0^\infty \rho^{2s-7}\tilde{f}_j^k(\rho,\theta)\,\mathrm{d}\rho = \frac{\rho^{2s-6}}{2s-6}\tilde{f}_j^k(\rho,\theta)\Big|_0^\infty - \frac{1}{2s-6}\int_0^\infty \rho^{2s-6}\partial_\rho \tilde{f}_j^k(\rho,\theta)\,\mathrm{d}\rho\\
&= -\frac{1}{2s-6}\int_0^\infty \rho^{2s-6}\partial_\rho \tilde{f}_j^k(\rho,\theta)\,\mathrm{d}\rho = \cdots = -\frac{1}{(2s-6)\cdots(2s-2)}\int_0^\infty \rho^{2s-2}\partial_\rho^5 \tilde{f}_j^k(\rho,\theta)\,\mathrm{d}\rho\\
&= \frac{\Gamma(2-2s)}{\Gamma(7-2s)}\int_0^\infty \rho^{2s-2}\partial_\rho^5 \tilde{f}_j^k(\rho,\theta)\,\mathrm{d}\rho,
\end{aligned} \tag{2.20}$$

Recall the integral identity (cf. [26, p. 440]):

$$\int_0^\infty x^{\mu-1}\sin(ax)\,\mathrm{d}x = \frac{\Gamma(\mu)}{a^\mu}\sin\Big(\frac{\mu\pi}{2}\Big),\quad a>0,\ \mu\in(0,1), \tag{2.21}$$

which holds for $\mu=0$ by understanding $\lim\limits_{\mu\to 0}\Gamma(\mu)\sin(\mu\pi/2)=\pi/2$. This corresponds to the Sine integral (cf. [26, p. 423]):

$$\int_0^\infty \frac{\sin(ax)}{x}\,\mathrm{d}x = \frac{\pi}{2},\quad a>0. \tag{2.22}$$

Then, by (2.19) and (2.21) with $\mu=2s-1$ (and (2.2) for $s=1/2$ and $\mu=0$), we obtain

$$\begin{aligned}
\int_0^\infty \rho^{2s-2}\partial_\rho^5 \tilde{f}_j^k(\rho,\theta)\,\mathrm{d}\rho &= -\frac{1}{32}\sum_{p,q=-2}^{2} c_p c_q \int_0^\infty \rho^{2s-2}\big((\alpha_{pq})^5\sin(\alpha_{pq}\rho)+(\beta_{pq})^5\sin(\beta_{pq}\rho)\big)\,\mathrm{d}\rho\\
&= -\frac{\Gamma(2s-1)}{32}\sin\Big(\frac{(2s-1)\pi}{2}\Big)\sum_{p,q=-2}^{2} c_p c_q\big((\alpha_{pq})^{6-2s}+(\beta_{pq})^{6-2s}\big)\\
&= \frac{\Gamma(2s-1)}{32}\cos(s\pi)\sum_{p,q=-2}^{2} c_p c_q\big((\alpha_{pq})^{6-2s}+(\beta_{pq})^{6-2s}\big),
\end{aligned} \tag{2.23}$$

which holds for $s=\frac{1}{2}$ with the understanding $\lim\limits_{s\to 1/2}\Gamma(2s-1)\cos(s\pi)=-\frac{\pi}{2}$.

Thus, we derive from (2.17), (2.20), and (2.23) that

$$\begin{aligned}
g_j^k(\theta) &= \frac{\Gamma(2-2s)\Gamma(2s-1)}{32\Gamma(7-2s)}\cos(s\pi)\sum_{p,q=-2}^{2} c_p c_q\big((\alpha_{pq})^{6-2s}+(\beta_{pq})^{6-2s}\big)\\
&= -\frac{1}{64\Gamma(7-2s)\sin(s\pi)}\sum_{p,q=-2}^{2} c_p c_q\big((\alpha_{pq})^{6-2s}+(\beta_{pq})^{6-2s}\big),
\end{aligned} \tag{2.24}$$

where in the last step, we used the property:

$$\Gamma(z)\Gamma(1-z) = \frac{\pi}{\sin \pi z},\quad z\neq 0,-1,\cdots. \tag{2.25}$$

(ii) $s\in(0,\frac{1}{2})$**:** Recall the integral identity (cf. [26, p. 441]):

$$\int_0^\infty x^{\mu-1}\cos(ax)\,\mathrm{d}x=\frac{\Gamma(\mu)}{a^\mu}\cos\Big(\frac{\mu\pi}{2}\Big),\quad a>0,\ \mu\in(0,1). \tag{2.26}$$

We integrate the equation (2.20) by parts one more time and obtain

$$g_j^k(\theta)=\int_0^\infty \rho^{2s-7}\tilde{f}_j^k(\rho,\theta)\,\mathrm{d}\rho=\frac{\Gamma(1-2s)}{\Gamma(7-2s)}\int_0^\infty \rho^{2s-1}\partial_\rho^6\tilde{f}_j^k(\rho,\theta)\,\mathrm{d}\rho. \tag{2.27}$$

Then, by (2.19) and (2.26) with $\mu=2s\in(0,1)$, we obtain

$$\begin{aligned}\int_0^\infty \rho^{2s-1}\partial_\rho^6\tilde{f}_j^k(\rho,\theta)\,\mathrm{d}\rho&=-\frac{1}{32}\sum_{p,q=-2}^{2}c_pc_q\int_0^\infty\rho^{2s-1}\big((\alpha_{pq})^6\cos(\alpha_{pq}\rho)+(\beta_{pq})^6\cos(\beta_{pq}\rho)\big)\,\mathrm{d}\rho\\&=-\frac{\Gamma(2s)}{32}\cos(s\pi)\sum_{p,q=-2}^{2}c_pc_q\big((\alpha_{pq})^{6-2s}+(\beta_{pq})^{6-2s}\big).\end{aligned}$$

Hence, following the same lines as the previous cases, we can derive (2.24) with $s\in(0,\frac{1}{2})$ similarly. A combination of (2.16), (2.18) and (2.24) leads to

$$S_{ll'}=\widetilde{C}_s\int_0^{\frac{\pi}{2}}\sum_{p,q=-2}^{2}c_pc_q\frac{|(j+p)\cos\theta+(k+q)\varrho\sin\theta|^{6-2s}+|(j+p)\cos\theta-(k+q)\varrho\sin\theta|^{6-2s}}{\cos^4\theta\sin^4\theta}\,\mathrm{d}\theta,$$

where $\widetilde{C}_s=\widehat{C}_sh_x^{4-2s}/h_y^2$ with $\widehat{C}_s$ given in (2.13). Introducing $f_j^k(\theta)$ in (2.12), we can rewrite the integral and then use a simple substitution to obtain

$$S_{ll'}=\widetilde{C}_s\int_0^{\frac{\pi}{2}}\big(f_j^k(\theta)+f_j^k(-\theta)\big)\,\mathrm{d}\theta=\widetilde{C}_s\Big(\int_0^{\frac{\pi}{2}}f_j^k(\theta)\,\mathrm{d}\theta+\int_{-\frac{\pi}{2}}^0 f_j^k(\theta)\,\mathrm{d}\theta\Big)=\widetilde{C}_s\int_{-\frac{\pi}{2}}^{\frac{\pi}{2}}f_j^k(\theta)\,\mathrm{d}\theta.$$

Finally, by the relation between the indices, that is, $l=(n-1)M+m$, $l'=(n'-1)M+m'$, $j=|m-m'|$, and $k=|n-n'|$, we can derive the desired formulas. $\square$

Remark 2.1. *Vollmann and Schulz* [42] *explored the multilevel Toeplitz structures of the FEM on rectangular meshes for general nonlocal operators with translation and reflection invariant kernels. In contrast to our approach, the implementation was performed in the physical space based on the hypersingular integral* (1.7).

We observe from the Toeplitz-structure of $\boldsymbol{S}$ that *it can be generated from the matrix* $\boldsymbol{G}\in\mathbb{R}^{MN}$ *with the entries* $G_{kj}=t_j^k$*, and the value of* t_j^k *only depends on the mesh ratio* ϱ *and the fractional order* s. In particular, if $h_x=h_y=h$ (i.e., $\varrho=1$), we can show that $t_j^k=t_k^j$ for $0\le j,k\le\min\{N,M\}-1$. In what follows, we shall restrict our attention to this case, but with different M,N. In fact, the algorithm can be extended to $h_x\neq h_y$ without difficulty.

As each entry can be computed independently, we do not specify the dependence of the notation on j,k and s. Denote

$$x_{j+p} := |j+p|h, \quad y_{k+q} := |k+q|h, \quad 0 \le j \le J := M-1,\, 0 \le k \le K := N-1, \tag{2.28}$$

for $p,q \in \{0,\pm 1,\pm 2\}$. The following alternative formulation of t_j^k is more convenient for computation.

Corollary 2.1. If $h_x = h_y = h$, then we can rewrite t_j^k in Theorem 2.1 as

$$t_j^k = \int_0^{\frac{\pi}{2}} F_j^k(\theta)\,\mathrm{d}\theta, \quad 0 \le j \le J,\, 0 \le k \le K, \tag{2.29}$$

where the integrand

$$F_j^k(\theta) = \frac{h^{-\gamma}}{\sin^4\theta\cos^4\theta} \sum_{p,q=-2}^{2} c_p c_q \Big\{ \big|x_{j+p}\sin\theta - y_{k+q}\cos\theta\big|^\gamma + \big|x_{j+p}\sin\theta + y_{k+q}\cos\theta\big|^\gamma \Big\}, \tag{2.30}$$

with $\gamma = 6-2s$ and $\{c_i\}$ given in (2.13). Moreover, we have $t_j^k = t_k^j$ for $0 \le j,k \le \min\{J,K\}$.

Proof. In view of (2.11)-(2.12), we make the change of variable $\theta \to -\theta$ for $\theta \in (-\pi/2,0)$ and obtain

$$\begin{aligned} t_j^k &= \int_{-\frac{\pi}{2}}^{\frac{\pi}{2}} f_j^k(\theta)\,\mathrm{d}\theta = \int_0^{\frac{\pi}{2}} \big(f_j^k(\theta) + f_j^k(-\theta)\big)\,\mathrm{d}\theta = \int_0^{\frac{\pi}{2}} \big(f_j^k(\pi/2-\theta) + f_j^k(\theta-\pi/2)\big)\,\mathrm{d}\theta \\ &= \int_0^{\frac{\pi}{2}} \big(f_k^j(\theta) + f_j^k(\theta-\pi/2)\big)\,\mathrm{d}\theta = \int_0^{\frac{\pi}{2}} \big(f_k^j(\pi/2-\theta) + f_j^k(\theta)\big)\,\mathrm{d}\theta := \int_0^{\frac{\pi}{2}} F_j^k(\theta)\,\mathrm{d}\theta, \end{aligned}$$

where we used the substitution $\theta \to \frac{\pi}{2} - \theta$ in the last step, and denoted the integrand by $F_j^k(\theta)$. Note from (2.30) that $F_j^k(\theta) = F_k^j(\pi/2-\theta)$, so we find from (2.29) immediately that $t_j^k = t_k^j$. $\square$

To conclude this section, we remark that the proposed approach can recover the standard FEM stiffness matrix:

$$\boldsymbol{S} = \boldsymbol{S}_x \otimes \boldsymbol{M}_y + \boldsymbol{M}_x \otimes \boldsymbol{S}_y, \tag{2.31}$$

where

$$\boldsymbol{S}_z = \frac{1}{h_z}\mathrm{diag}(-1,2,-1), \quad \boldsymbol{M}_z = \frac{h_z}{6}\mathrm{diag}(1,4,1), \quad z = x,y,$$

are the usual tridiagonal FEM stiffness and mass matrices in one dimension, respectively. When $s=1$, the factor $(\xi^2+\eta^2)^s$ is separable, so we derive from (2.15) and direction calculation that

$$S_{ll'} = \frac{16}{\pi^2 h_x^2 h_y^2} \Big(\int_0^\infty \frac{w(\xi;j,h_x)}{\xi^2}\,\mathrm{d}\xi \int_0^\infty \frac{w(\eta;k,h_y)}{\eta^4}\,\mathrm{d}\eta + \int_0^\infty \frac{w(\xi;j,h_x)}{\xi^4}\,\mathrm{d}\xi \int_0^\infty \frac{w(\eta;k,h_y)}{\eta^2}\,\mathrm{d}\eta \Big),$$

where

$$w(x;\ell,h)=\frac{1}{4}\sum_{p=-2}^{2}c_p\cos((\ell+p)hx).$$

Using integration by parts, we find

$$\int_0^\infty \frac{w(x;\ell,h)}{x^2}\mathrm{d}x=-\frac{h}{4}\sum_{p=-2}^{2}c_p(\ell+p)\int_0^\infty \frac{\sin((\ell+p)hx)}{x}\mathrm{d}x=-\frac{\pi h}{8}\sum_{p=-2}^{2}c_p|\ell+p|,$$

$$\int_0^\infty \frac{w(x;\ell,h)}{x^4}\mathrm{d}x=\frac{h^3}{24}\sum_{p=-2}^{2}c_p(\ell+p)^3\int_0^\infty \frac{\sin((\ell+p)hx)}{x}\mathrm{d}x=\frac{\pi h^3}{48}\sum_{p=-2}^{2}c_p|\ell+p|^3,$$

where we used the formula (2.2) (see [26, P. 423]): for $a\in\mathbb{R}$,

$$\int_0^\infty \frac{\sin(ax)}{x}\mathrm{d}x=\frac{\pi}{2}\mathrm{sign}(a).$$

One verifies readily that

$$\sum_{p=-2}^{2}c_p|z+p|=\begin{cases}-4, & \text{if } z=0,\\ 2, & \text{if } z=1,\\ 0, & \text{if } z\geq 2,\end{cases}\qquad \sum_{p=-2}^{2}c_p|z+p|^3=\begin{cases}8, & \text{if } z=0,\\ 2, & \text{if } z=1,\\ 0, & \text{if } z\geq 2.\end{cases}$$

A combination of the above leads to the assembled matrix form given in (2.31).

3 Fast and accurate computation of the one-dimensional integral t_j^k

In this section, we describe the algorithm for computing the one-dimensional integrals $\{t_j^k\}$ in (2.29)-(2.30). Note that their values only depend on the fractional order s, and it suffices to compute $\{t_j^k\}$ with $j\geq k\geq 0$ (as $t_j^k=t_k^j$), and $J\geq K$. Indeed, for $J\leq K$, the generating matrix can be obtained by the transpose $\boldsymbol{G}^t$. As a result, we always assume that

$$j\geq k\geq 0,\quad 0\leq j\leq J,\quad 0\leq k\leq K\leq J. \tag{3.1}$$

The main focus will be placed on how to deal with the singularities of the integrand $F_j^k(\theta)$. As shown in Fig. 1, $F_j^k(\theta)$ exhibits some local steep peaks that need to be located and resolved.

We find from (2.30) readily that $F_j^k(\theta)$ has a low regularity at θ satisfying $x_{j+p}\sin\theta-y_{k+q}\cos\theta=0$, but $x_{j+p}\neq 0, y_{k+q}\neq 0$, that is, at

$$\vartheta_p^q:=\arctan\Big(\frac{y_{k+q}}{x_{j+p}}\Big)=\arctan\Big(\frac{|k+q|}{|j+p|}\Big)\in(0,\pi/2),\quad \forall p\in\Upsilon_j,\forall q\in\Upsilon_k, \tag{3.2}$$

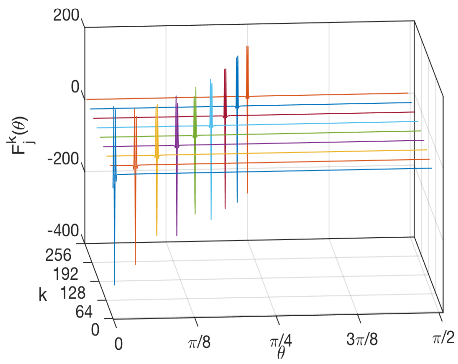

(a) $j=256$, $k=0:32:256$.

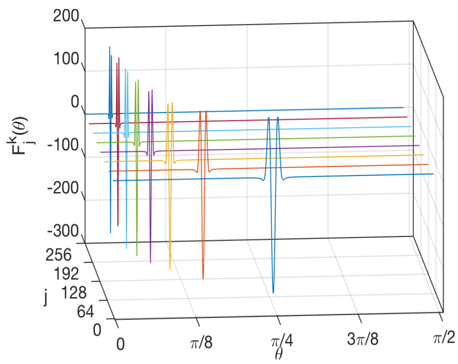

(b) $k=32$, $j=32:32:256$.

Figure 1: Profiles of $F_j^k(\theta)$ with $\theta\in[0,\pi/2]$ for $s=0.7$.

where the index set

$$\Upsilon_\ell=\{i:i\in\{0,\pm1,\pm2\},i\neq-\ell\},\quad \ell\geq 0. \tag{3.3}$$

Based on the location and nature of the singularities, we split the integral (2.29) into

$$\begin{aligned} t_j^k&=\int_0^{\theta_1}F_j^k(\theta)\,\mathrm{d}\theta+\int_{\theta_1}^{\theta_2}F_j^k(\theta)\,\mathrm{d}\theta+\int_{\theta_2}^{\frac{\pi}{2}}F_j^k(\theta)\,\mathrm{d}\theta\\ &:=\mathcal{I}_j^k(\theta_1)+\mathcal{J}_j^k(\theta_1,\theta_2)+\mathcal{I}_k^j(\pi/2-\theta_2), \end{aligned} \tag{3.4}$$

where $0<\theta_1<\theta_2<\pi/2$ are two constants to be specified later such that all the interior "singular" points $\vartheta_p^q\in(\theta_1,\theta_2)$. Here the relation between the first and third integrals in (3.4) follows from a simple change of variable and the property $F_k^j(\theta)=F_j^k(\pi/2-\theta)$. We proceed to compute $\mathcal{I}_j^k(\theta_1)$ by using the binomial expressions at $\theta=0,\pi/2$, and $\mathcal{J}_j^k(\theta_1,\theta_2)$ by a suitable Jacobi-Gauss quadrature where the weight function is chosen to absorb the interior "singularities" of the integrand.

3.1 Computation of $\mathcal{I}_j^k(\theta_1)$

To reduce the roundoff errors in computation (particularly for $j\gg k$), we adopt the normalisation

$$\bar{x}_{j+p}:=\frac{x_{j+p}}{x_{j+2}}=\frac{|j+p|}{j+2}\leq 1,\quad \bar{y}_{k+q}:=\frac{y_{k+q}}{y_{k+2}}=\frac{|k+q|}{k+2}\leq 1,\quad \forall p\in\Upsilon_j,\forall q\in\Upsilon_k, \tag{3.5}$$

and define the normalised sine and cosine as

$$\mathcal{S}_j(\theta):=x_{j+2}\sin\theta,\quad \mathcal{C}_k(\theta):=y_{k+2}\cos\theta. \tag{3.6}$$

For simplicity, we introduce two constants involved in the following proposition:

$$C_{2n}^{j,k} := \Big(\sum_{|p|=0}^{2} c_p \bar{x}_{j+p}^{2n+4}\Big)\Big(\sum_{q\in\Upsilon_k} c_q \bar{y}_{k+q}^{2-2n-2s}\Big), \quad \widetilde{C}^{j,k} := \begin{cases} c_{-k} \sum_{|p|=0}^{2} c_p \bar{x}_{j+p}^{\gamma}, & \text{if } k\le 2, \\ 0, & \text{if } k\ge 3. \end{cases} \tag{3.7}$$

We can compute $\mathcal{I}_j^k(\theta_1)$ by the following binormal expansion which indicates the singularity of $F_j^k(\theta)$ in (2.29) at $\theta=0$ is removable.

Proposition 3.1. Let $s\in(0,1)$. If $\tan\vartheta<\tan\vartheta_p^q$, i.e., $0\le\vartheta<\vartheta_p^q$ for all $p\in\Upsilon_j, q\in\Upsilon_k$, then

$$\mathcal{I}_j^k(\vartheta)=\int_0^{\vartheta} F_j^k(\theta)\,\mathrm{d}\theta=\frac{2x_{j+2}^4 y_{k+2}^4}{h^{\gamma}}\Big\{\widetilde{C}^{j,k}\widetilde{R}(\vartheta)+\sum_{n=0}^{\infty}\frac{(\gamma)_{2n+4}C_{2n}^{j,k}}{(2n+4)!}R_{2n}(\vartheta)\Big\}, \tag{3.8}$$

where $\gamma=6-2s$, $(\gamma)_m=\gamma(\gamma-1)\cdots(\gamma-m+1)$ is the counting down Pochhammer symbol, and

$$R_{2n}(\vartheta):=\int_0^{\vartheta}\frac{(\mathcal{S}_j(\theta))^{2n}}{(\mathcal{C}_k(\theta))^{2n+2+2s}}\mathrm{d}\theta, \quad \widetilde{R}(\vartheta):=\int_0^{\vartheta}\frac{(\mathcal{S}_j(\theta))^{2-2s}}{(\mathcal{C}_k(\theta))^{4}}\mathrm{d}\theta, \tag{3.9}$$

with the constants $C_{2n}^{j,k}$ and $\widetilde{C}^{j,k}$ given in (3.7). Moreover, we have the recurrence relation

$$R_{2n-2}(\vartheta)=-\frac{2n+1+2s}{2n-1}\Big(\frac{k+2}{j+2}\Big)^2 R_{2n}(\vartheta)+\frac{1}{2n-1}\,\frac{k+2}{j+2}\,\frac{(\mathcal{S}_j(\vartheta))^{2n-1}}{(\mathcal{C}_k(\vartheta))^{2n+1+2s}}, \tag{3.10}$$

and the explicit representation

$$\widetilde{R}(\vartheta)=\frac{\sin(2\vartheta)(1+2s\cos^2\vartheta)}{6}\,\frac{(\mathcal{S}_j(\vartheta))^{2-2s}}{(\mathcal{C}_k(\vartheta))^4}+\frac{2s(s-1)}{3}\,\frac{x_{j+2}^{2-2s}}{y_{k+2}^4}B(\sin^2\vartheta;3/2-s,1/2), \tag{3.11}$$

where $B(x;a,b)$ is the incomplete Beta function.

We sketch the derivation in Appendix A to avoid distraction from the main topic. Note that the expansion (3.8) is valid for all

$$0\le\vartheta<\vartheta_{\min}^{j,k}:=\min_{p,q}\big\{\vartheta_p^q : p\in\Upsilon_j, q\in\Upsilon_k\big\}=\begin{cases}\arctan\big(\frac{k-2}{j+2}\big), & \text{if } k\ge 3,\\ \arctan\big(\frac{1}{j+2}\big), & \text{if } 0\le k\le 2.\end{cases} \tag{3.12}$$

In practice, we have to truncate the infinite sum and approximate $\mathcal{I}_j^k(\vartheta)$ by

$$\widetilde{\mathcal{I}}_j^k(\vartheta)=\frac{2x_{j+2}^4 y_{k+2}^4}{h^{\gamma}}\Big\{\widetilde{C}^{j,k}\widetilde{R}(\vartheta)+\sum_{n=0}^{N_\delta-1}\frac{(\gamma)_{2n+4}C_{2n}^{j,k}}{(2n+4)!}R_{2n}(\vartheta)\Big\}, \tag{3.13}$$

where the cut-off number N_δ can be determined by the truncation error for some $0<\delta<1$ and under the condition

$$\frac{x_{j+p}\sin\vartheta}{y_{k+q}\cos\vartheta}\le\delta<1, \text{ i.e., } 0\le\vartheta\le\arctan(\delta\vartheta_{\min}^{j,k}):=\theta_1. \tag{3.14}$$

Proposition 3.2. Let $s \in (0,1)$ and let $\delta \in (0,1)$ be given. Then under the condition (3.14), we have the truncation error

$$\big|\mathcal{I}_j^k(\vartheta) - \widetilde{\mathcal{I}}_j^k(\vartheta)\big| \le \widehat{C}_{j,k}^s(\vartheta)\, \frac{\mathrm{e}^{-2|\ln\delta| N_\delta}}{|\ln\delta|\, N_\delta^{7-2s}}, \tag{3.15}$$

where

$$\widehat{C}_{j,k}^s(\vartheta) := \frac{c\Gamma(7-2s)|\sin(2s\pi)|\vartheta}{2^{6-2s}\pi(\cos\vartheta)^{2+2s}} \Big(\sum_{|p|=0}^{2} |c_p||j+p|^4\Big)\Big(\sum_{q\in\Upsilon_k} |c_q||k+q|^{2-2s}\Big), \quad c\approx 1.$$

We sketch the proof in Appendix B. With the above estimate, we can determine N_δ for a preassigned $\delta\in(0,1)$ and a given error tolerance to compute $\mathcal{I}_j^k(\theta_1)$, so does $\mathcal{I}_k^j(\pi/2-\theta_2)$ with $\theta_2 = \pi/2-\theta_1$ in a fast manner. In Fig. 2, we depict the subinterval $[\theta_1,\theta_2]\subset[0,\pi/2]$ for fixed j or k with $\delta = 0.9$ and $s = 0.7$, where in the shaded region, we need to compute $\mathcal{J}_j^k(\theta_1,\theta_2)$.

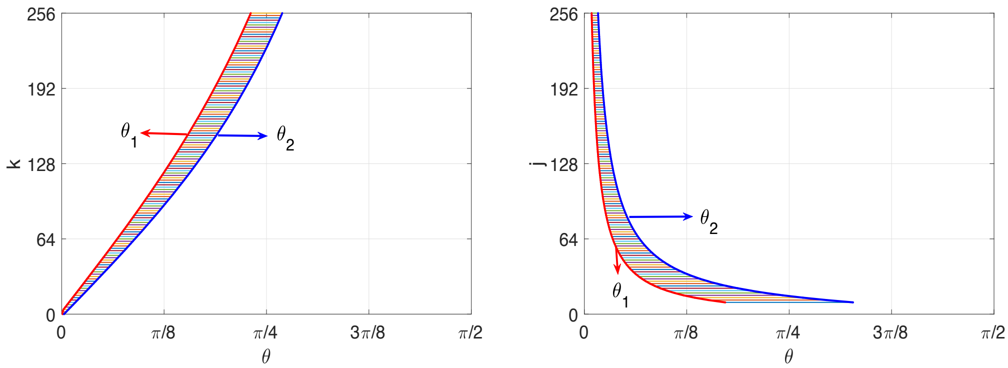

(a) $j = 256$ and $k = 0{:}256$.

(b) $k = 10$ and $j = 10{:}256$.

Figure 2: The distribution of the subinterval $[\theta_1,\theta_2]$ with $\delta = 0.9$ and $s = 0.7$.

3.2 Computation of $\mathcal{J}_j^k(\theta_1,\theta_2)$

As illustrated in Fig. 1, the peaks (resulted from local singularities) of the integrand $F_j^k(\theta)$ in (2.30) are contained in $[\theta_1,\theta_2]$. We can show that such singularities can be absorbed by the weight function of a suitable Jacobi-Gauss quadrature. To this end, we introduce the linear transformation:

$$w_1(z) = \frac{\theta_1 - \vartheta_p^q}{2} z + \frac{\vartheta_p^q + \theta_1}{2} \in (\theta_1, \vartheta_p^q), \quad w_2(z) = \frac{\theta_2 - \vartheta_p^q}{2} z + \frac{\vartheta_p^q + \theta_2}{2} \in (\vartheta_p^q, \theta_2), \tag{3.16}$$

for $z \in (-1,1)$, where ϑ_p^q is defined in (3.2). Define

$$d_1 = \frac{\vartheta_p^q - \theta_1}{2}, \quad d_2 = \frac{\theta_2 - \vartheta_p^q}{2}. \tag{3.17}$$

Proposition 3.3. For $s\in(0,1)$ and fixed $j\geq k\geq 0$, $\mathcal{J}_j^k(\theta_1,\theta_2)$ in (3.4) can be computed by

$$\mathcal{J}_j^k(\theta_1,\theta_2)=\frac{16}{h^\gamma}\sum_{p,q=-2}^{2}c_pc_q(x_{j+p}^2+y_{k+q}^2)^{\frac{\gamma}{2}}\mathcal{I}_{p,q}, \tag{3.18}$$

where for $j\geq k\geq 3$,

$$\begin{aligned}\mathcal{I}_{p,q}=\mathcal{I}_{p,q}^-+\mathcal{I}_{p,q}^+:=&\int_{-1}^{1}\Big\{\Big(\frac{\sin(d_1(1+z))}{d_1(1+z)}\Big)^\gamma\frac{d_1^{\gamma+1}(1+z)^5}{\sin^4(2w_1(z))}\\&+\Big(\frac{\sin(d_2(1+z))}{d_2(1+z)}\Big)^\gamma\frac{d_2^{\gamma+1}(1+z)^5}{\sin^4(2w_2(z))}\Big\}(1+z)^{1-2s}\mathrm{d}z+\int_{\theta_1}^{\theta_2}\frac{|\sin(\theta+\vartheta_p^q)|^\gamma}{\sin^4(2\theta)}\mathrm{d}\theta,\end{aligned} \tag{3.19}$$

while for $j\geq k$ and $k\leq 2$,

$$\mathcal{I}_{p,q}=\frac{2y_{k+2}^4}{x_{j+2}^{2-2s}}\big(\widetilde{R}(\theta_2)-\widetilde{R}(\theta_1)\big), \tag{3.20}$$

and for $2\geq j\geq k\geq 0$,

$$\mathcal{I}_{p,q}=\frac{2y_{k+2}^4}{x_{j+2}^{2-2s}}\big(\widetilde{R}(\pi/2-\theta_2)-\widetilde{R}(\pi/2-\theta_1)\big). \tag{3.21}$$

Here $\widetilde{R}(\theta)$ is computed explicitly by (3.11).

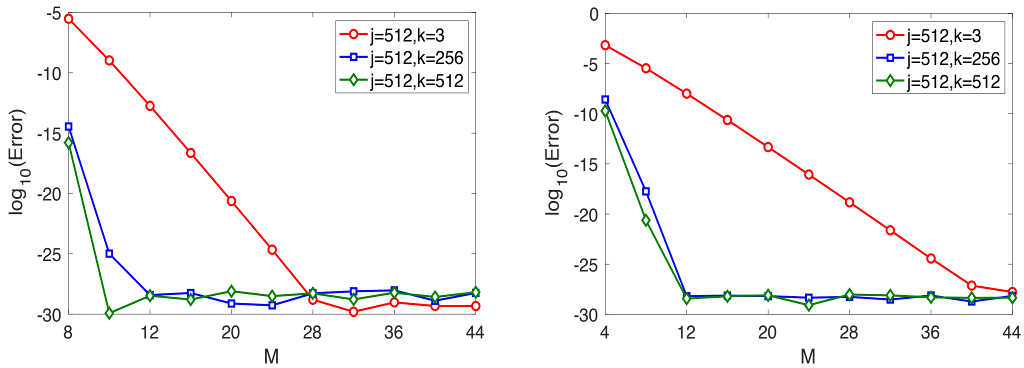

Figure 3: Maximum errors of quadrature against number of nodes with $s=0.7$. Left: Jacobi-Gauss quadrature for $\mathcal{I}_{p,q}^-$. Right: Legendre-Gauss quadrature for $\mathcal{I}_{p,q}^+$.

We refer to Appendix C for the derivation. It is seen from (3.19) that the integrals $\mathcal{I}_{p,q}^-$ can be computed very accurately by using the Jacobi-Gauss quadrature with the weight $\omega^{(0,1-2s)}(z)=(1+z)^{1-2s}$ and a small number of nodes. Meanwhile, the integral $\mathcal{I}_{p,q}^+$ can be evaluated accurately by the Legendre-Gauss quadrature with a small number of nodes as well. In Fig. 3, we show the maximum quadrature errors for several j,k with the reference values obtained by a large enough number of nodes. In the worst case with $j \gg k$, we need slightly more nodes than the case when j,k are close. Here, we resort to the Multiprecision Computing Toolbox for Matlab [1] in some extreme cases, so we observe the accuracy up to 10^{-30}.

We summarise the algorithm for computing the entries $\{t_j^k\}$ of the generating matrix $\boldsymbol{G}$ as follows.

Algorithm 1: Evaluate t_j^k

for $k=0,\cdots,K$ **do**
  for $j=k,\cdots,J$ **do**
    Set θ_1 to be the value in (3.14) and $\theta_2=\frac{\pi}{2}-\theta_1$;
    Compute $\widetilde{\mathcal{I}}_j^k(\theta_1)$ and $\widetilde{\mathcal{I}}_k^j(\pi/2-\theta_2)$ by (3.13);
    Compute $\mathcal{J}_j^k(\theta_1,\theta_2)$ by (3.18) and the quadrature rule to obtain $\widetilde{\mathcal{J}}_j^k(\theta_1,\theta_2)$;
    Set
$$t_j^k=\widetilde{\mathcal{I}}_j^k(\theta_1)+\widetilde{\mathcal{J}}_j^k(\theta_1,\theta_2)+\widetilde{\mathcal{I}}_k^j(\pi/2-\theta_2).$$
  end
end

3.3 Decay rate of t_j^k and sparsity of the generating matrix

With the analytic formula of t_j^k in Theorem 2.1 at our disposal, we can show that the entries $\{t_j^k\}$ of the generating matrix $\boldsymbol{G}$ decay at a rate $O((j^2+k^2)^{-(s+1)})$. As a result, for a given error tolerance (e.g., $O(h^3)$), the entries with large j or k can be set as zero, so the matrix $\boldsymbol{G}$ becomes relatively "sparse" (see Fig. 4). The derivation of the following decay rate is essentially based on an alternative representation of the integrand $f_j^k(\theta)$ in (2.12) derived from the finite difference perspective, which is sketched in Appendix D.

Proposition 3.4. For $s\in(0,1)$ and $h_x=h_y=h$, the integral t_j^k in (2.11) behaves like

$$t_j^k=O\big((j^2+k^2)^{-(s+1)}\big), \tag{3.22}$$

where the constant in the O-term is independent of j, k and h.

In Fig. 4 (left), we plot the magnitude of the diagonal entries (i.e., $|t_j^k|$ with $j=k$) of $\boldsymbol{G}$ against the reference decay rate $(j^2+k^2)^{-(s+1)}$ by (3.22) for different s, which shows a good agreement. In actual computation, we can directly set t_j^k with small magnitudes to be zero. More precisely, if the magnitude of the entry of the stiffness matrix $\boldsymbol{S}$ is smaller than h^3, we set it to be zero. Indeed, by (2.10), $\boldsymbol{S}$ is generated by $\boldsymbol{G}$ with its entry multiplying the factor $\widehat{C}_s h^{2-2s}$, so we can adopt the truncation rule: if $|t_j^k|<h^{2s+1}$, then we set $t_j^k=0$.

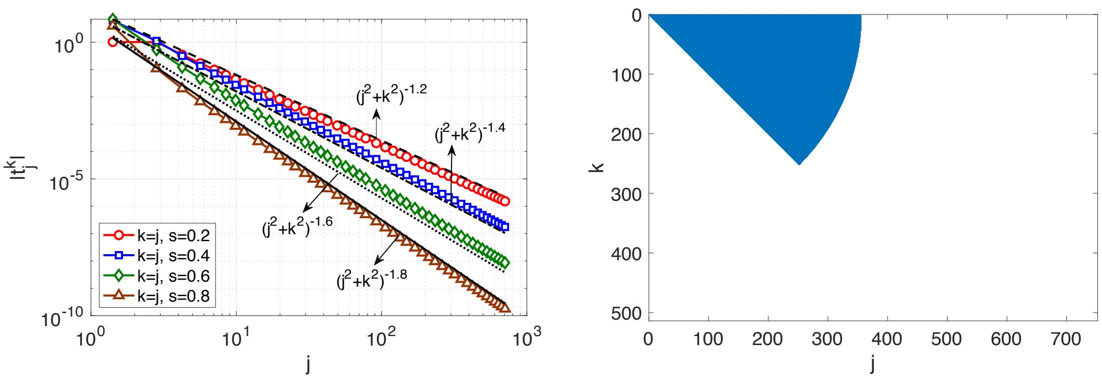

Figure 4: Left: Decay rate of $|t_j^k|$ with $k=j$ various s. Right: Portion of $\{t_j^k\}$ for $1\le j\le J=750$ and $1\le k\le K=512$ needs to be evaluated, where $s=0.3$.

In view of (3.22), we require $\sqrt{j^2+k^2}\ge h^{\frac{1}{2(s+1)}-1}$. In practice, it is safe to set $t_j^k=0$ for all $\sqrt{j^2+k^2}>P:=[c(s)h^{-(1+\epsilon)}]$ (the integer part) for some small $\epsilon>0$ and $0<c(s)<1$. In fact, we find from many tests that a good choice is $\epsilon=0.07$ and $c(s)=1-0.18s$, so we take these values in what follows. We illustrate in Fig. 4 (right) the nonzero entries of the modified generating matrix $\boldsymbol{G}$ with $j\ge k$ and $\sqrt{j^2+k^2}\le P=357$, where $s=0.3$, $h=2^{-8}$, $J=750$, $K=512$. In fact, about 14% of $\{t_j^k\}$ is needed to be evaluated in view of the symmetry and decay properties.

In Table 1, we tabulate the sparsity of modified generating matrix (i.e., the number of zero entries divided by the total number of entries) for $J=K=2/h$ and various s and h, which indicates a substantial saving can be gained. The condition number $\kappa(\boldsymbol{S})$ with/without cut-off for $s=0.3,0.7$ are depicted in Fig. 5, where both are consistent with the theoretical results $\kappa(\boldsymbol{S})=O(h^{-2s})$ (cf. [5, Theorem 5]).

Although more delicate analysis can be conducted for the cut-off rule, the above numerical evidences demonstrate that the h^3-rule can be used in practice.

Table 1: Sparsity of the generating matrix $\boldsymbol{G}$ for various s and h

	$s=0.2$		$s=0.3$		$s=0.4$		$s=0.6$		$s=0.7$		$s=0.8$	
h	P	Sparsity	P	Sparsity	P	Sparsity	P	Sparsity	P	Sparsity	P	Sparsity
2^{-3}	8	80.7%	8	80.7%	8	80.7%	8	80.7%	8	80.7%	7	85.2%
2^{-4}	18	75.3%	18	75.3%	18	75.3%	17	78.1%	16	80.3%	16	80.3%
2^{-5}	39	70.9%	38	72.7%	37	73.7%	36	75.6%	35	76.5%	34	77.8%
2^{-6}	82	67.8%	81	68.6%	79	70.8%	76	72.3%	74	73.7%	73	74.4%
2^{-7}	173	64.9%	170	65.5%	166	67.9%	160	69.9%	157	70.5%	153	71.9%
2^{-8}	363	60.5%	357	61.9%	350	63.5%	336	66.1%	329	67.6%	323	68.6%
2^{-9}	763	56.4%	749	58.0%	735	59.8%	706	62.7%	692	64.1%	678	65.5%

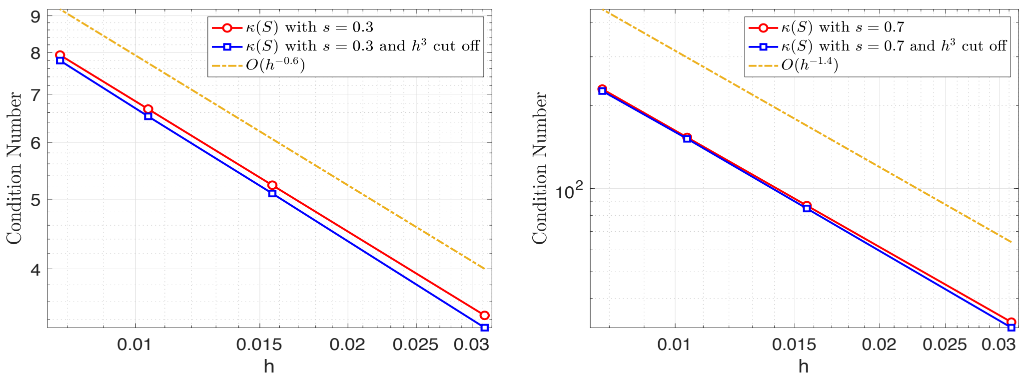

Figure 5: Condition Number for fractional stiffness matrix S with/without cutting off. Left: $s=0.3$. Right: $s=0.7$.

Remark 3.1. *It is noteworthy that there is much recent interest and attempt in sparse approximation of the IFL stiffness matrix. Karkulik and Melenk [29] developed a conforming FEM on the quasiuniform mesh based on the Caffarelli-Silvestre extension, where the individual blocks of the inverse of stiffness matrix can be approximated by low-rank matrices with an exponentially small error in the rank. Boukaram et al. [14] proposed the hierarchical matrix approximation to reduce the cost of storage requirement and matrix-vector multiplication as the full representation of the stiffness matrix is not affordable. We also refer to the references therein for some relevant approaches, though our method is different from these existing ones.*

4 Applications and numerical results

In this section, we consider several examples of PDEs with fractional Laplacian and show the accuracy and efficiency of the algorithm for computing the FEM stiffness matrix. We start with the fractional Poisson equation in rectangular and L-shaped domains, and then turn to the fractional-in-space Allen-Cahn equation.

4.1 Fractional Poisson equation on a rectangular domain

We first consider the model problem (1.3) with the weak form (2.4) and finite-element approximation (2.5). The convergence rate of the finite element approximation to (1.3) has been intensively studied in a more general setting (see, e.g., [4,10–12,25]). Here, we collect the most relevant estimates summarised in [6] (with original reference to [4,11]), in order to demonstrate that our solver can achieve the expected accuracy.

Theorem 4.1. *Let Ω be a rectangular domain with a mesh $\mathcal{T}_h$ defined in* (2.1)*, and let u,u_h be the solution to* (2.4) *and* (2.5)*, respectively. If f has the following regularity for different ranges* *of* $s\in(0,1)$, *then we have*

$$\|u-u_h\|_{\widetilde{H}^s(\Omega)}\leq C\begin{cases} h^{\frac{1}{2}}|\log h|\,\|f\|_{C^{\frac{1}{2}-s}(\bar{\Omega})}, & \text{if } s\in(0,1/2),\\ h^{\frac{1}{2}}|\log h|\,\|f\|_{L^\infty(\Omega)}, & \text{if } s=1/2,\\ h^{\frac{1}{2}}\sqrt{|\log h|}\,\|f\|_{C^\beta(\bar{\Omega})}, & \text{if } s\in(1/2,1),\end{cases} \tag{4.1}$$

where $h=\max\{h_x,h_y\}$ *and the constant* C *depends on the domain* Ω,s *and/or* β.

On the other hand, if $u\in H^{s+1/2-\varepsilon}(\Omega)$ *for any* $\varepsilon>0$, *we have*

$$\|u-u_h\|_{L^2(\Omega)}\leq C\begin{cases} h^{\frac{1}{2}+s-\varepsilon}|u|_{H^{s+\frac{1}{2}-\varepsilon}(\Omega)}, & \text{if } 0<s<1/2,\\ h^{1-2\varepsilon}|u|_{H^{s+\frac{1}{2}-\varepsilon}(\Omega)}, & \text{if } 1/2\leq s<1,\end{cases} \tag{4.2}$$

where the positive constant C *depends on the domain* Ω,s, *and* ε.

Here, the fractional Sobolev space $H^s(\Omega)$ is defined as in [35]. Note that it has a close relation with the fractional space $\widetilde{H}^s(\Omega)=\{v\in H^s(\mathbb{R}^2): v=0 \text{ in } \Omega^c\}$ (cf. [33, Chapter 3]): (i) for $s>1/2$, $\widetilde{H}^s(\Omega)$ coincides with the space $H_0^s(\Omega)$ which is the closure of $C_0^\infty(\Omega)$ with respect to the $H^s(\Omega)$-norm; (ii) for $s<1/2$, $\widetilde{H}^s(\Omega)$ is identical to $H^s(\Omega)$; and (iii) for $s=1/2$, $\widetilde{H}^s(\Omega)\subset H_0^s(\Omega)$, where the inclusion is strict. Note that the same regularity estimates on the solution u are derived in [13], but under much less restrictive assumptions on source function f.

Now we provide some numerical results and first test the algorithm for (1.3) with an "exact" solution. According to [38, 40, 41], we can compute the fractional Laplacian of a special function for $s>0$,

$$(-\Delta)^s\{e^{-\frac{\lambda^2\|\boldsymbol{x}\|^2}{2}}\}=2^s\lambda^{2s}\Gamma(s+1)\,{}_1F_1(s+1,1,-\lambda^2\|\boldsymbol{x}\|^2/2):=f_\lambda(\|\boldsymbol{x}\|),\ \boldsymbol{x}\in\mathbb{R}^2, \tag{4.3}$$

where ${}_1F_1(\cdot;\cdot;z)$ is the confluent hypergeometric function as in [36]. As a result, given $f_\lambda(\|\boldsymbol{x}\|)$ with $\boldsymbol{x}\in\Omega=(-1,1)^2$, we can choose a relatively large $\lambda>0$ such that $u_\lambda(\boldsymbol{x}):=e^{-\lambda^2\|\boldsymbol{x}\|^2/2}\approx 0$ for $\boldsymbol{x}\in\Omega^c$. In this case, both u_λ and f_λ are sufficiently smooth in $\mathbb{R}^2$, so we expect the FEM approximation can achieve the optimal second-order convergence for any $s\in(0,1)$, if the stiffness matrix is computed with a satisfactory accuracy. In the test, we take $\lambda=12$. In Fig. 6, we plot in log-log scale the L^∞-, L^2-, and H^s-errors with $s=0.4,0.6$, where we adopt the truncation rule in Table 1 to reduce computational cost. Indeed, we observe from Fig. 6 the optimal second-order convergence in all cases.

Next, we consider (1.3) with $f(\boldsymbol{x})=1$ and $\Omega=(0,1)^2$. We infer from [27, (7.12)] that the solution of (1.3) is singular near the boundary $\partial\Omega$ which behaves like

$$u(\boldsymbol{x})=\operatorname{dist}(\boldsymbol{x},\partial\Omega)^s v(\boldsymbol{x}), \tag{4.4}$$

where $\operatorname{dist}(\boldsymbol{x},\partial\Omega)$ denotes the distance from $\boldsymbol{x}\in\Omega$ to $\partial\Omega$ and v is a smooth function. Indeed, the solution has a regularity as in Theorem 4.1 (cf. [4]). In Fig. 7, we plot u_h on

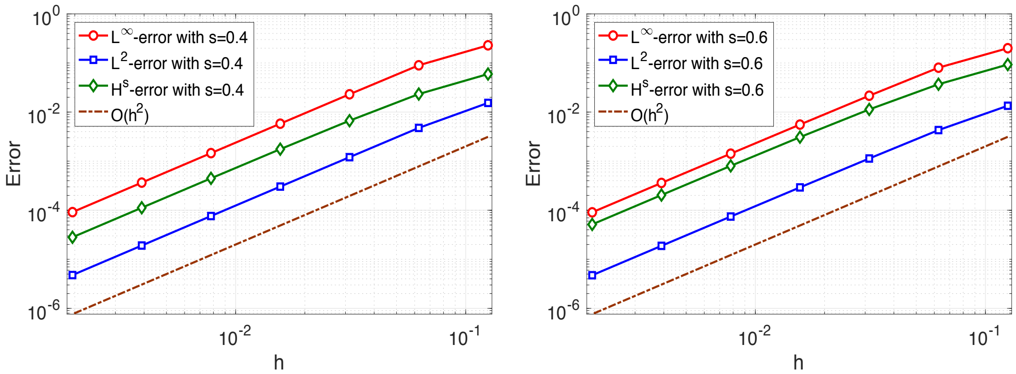

Figure 6: Errors and convergence order of FEM approximation to (1.3) with an "exact" solution given in (4.3). Left: $s=0.4$. Right: $s=0.6$.

sufficiently fine meshes generated by $M=N=2^{10}$ (i.e., $h_x=h_y=h=2^{-10}$) for $s=0.3,0.7$, and observe the singular layers near the boundary which are thinner and sharper for smaller s. Moreover, we shall use this as a reference solution to measure the numerical errors below.

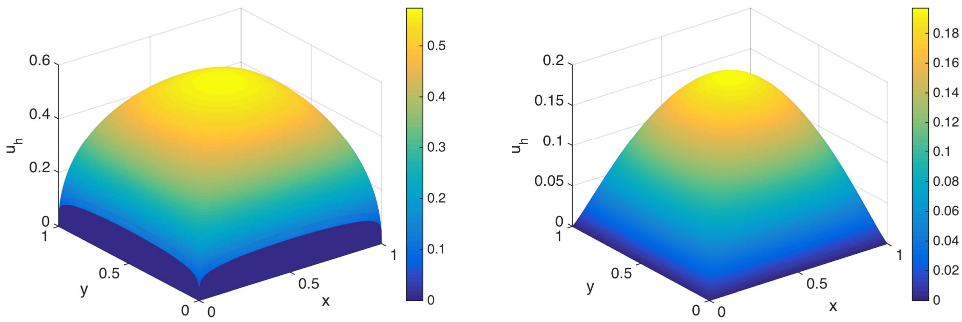

Figure 7: Profiles of the FEM solution u_h obtained by $M=N=2^{10}$. Left: $s=0.3$. Right: $s=0.7$.

In Fig. 8, we plot the errors in different norms against h for $s=0.2,0.3,0.4,0.6,0.7,0.8$ in log-log scale. Indeed, we observe from Fig. 8 (left) that the L^2-errors behave like the prediction in (4.2), that is, roughly of the order $O(h^{s+1/2})$ for $0<s<1/2$, and $O(h)$ for $1/2<s<1$. Similarly, Fig. 8 (middle) shows that the errors in H^s-norm agree with the estimates in (4.1), that is, approximately $O(h^{1/2})$. We also depict the L^∞-errors in Fig. 8 (right) which shows a slightly higher convergence order than the finite difference approximation in [24, 28] for the same example. We observe the convergence $O(h^{s+\gamma})$ with some $\gamma\approx 0.2$ for the FEM versus $O(h^s)$ for the finite difference. Moreover, we plot the numerical error plots for $s=0.1,0.5,0.99$ in Fig. 9, together with the integer case $s=1$ for comparison. We observe that numerical errors under L^2-norm and H^s-norm are in agreement with the theoretical predictions as expected for $s=0.01$ and $s=0.5$, and the convergence behavior up to the second order as $s\to 1$.

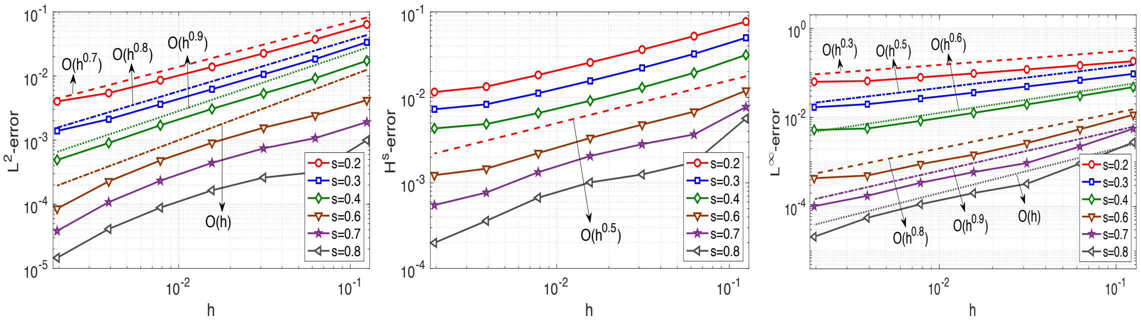

Figure 8: Errors and convergence order of FEM approximation to (1.3) with $f(\boldsymbol{x})=1$. Left: L^2-error. Middle: H^s-error. Right: L^∞-error.

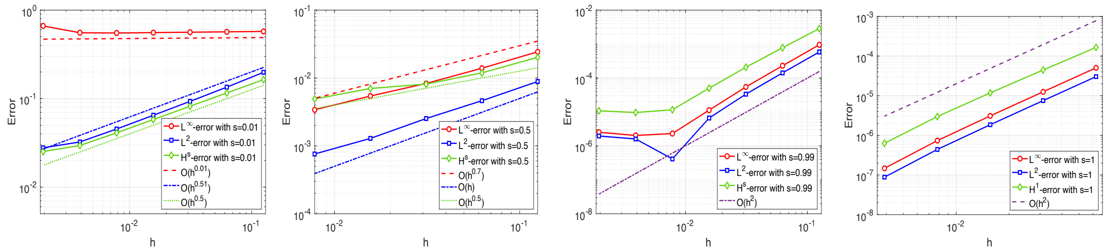

(a) $s=0.01$ (b) $s=0.5$ (c) $s=0.99$ (d) $s=1$

Figure 9: Errors and convergence order of FEM approximation to (1.3) with $f(\boldsymbol{x})=1$. From left to right: $s=0.01$, $s=0.5$, $s=0.99$, and $s=1$.

4.2 Fractional Poisson equation on an L-shaped domain

We next show that the FEM solver can be extended to a bounded domain that can be partitioned by nonoverlapping rectangular meshes. To fix the idea, we consider an L-shaped domain $\Omega=\Omega_1\cup\Omega_2\cup\Omega_3$ with each Ω_i being a square (see Fig. 10 (left)). We partition it by a uniform mesh, label all the "interior" first and then "edge" nodes in order. For notational clarity, we denote by N_d the total degrees of freedom, and by M,N the number of nodes in the x- and y-direction respectively. We further denote by $\widetilde{M},\widetilde{N}$ the number of "interior" nodes for each sub-domain Ω_i in x-direction and y-direction, respectively. Thus, we have $M=2\widetilde{M}+1$, $N=2\widetilde{N}+1$ and the degrees of freedom $N_d=3\widetilde{M}\widetilde{N}+\widetilde{M}+\widetilde{N}$. Accordingly, for the partition in Fig. 10 (right), we have $M=N=5,\widetilde{M}=\widetilde{N}=2$ and $N_d=16$. The l-th basis function on Ω is given by

$$\varphi_l(\boldsymbol{x})=\phi_m(x)\phi_n(y),\ 1\le l\le N_d, \tag{4.5}$$

where $\phi_\ell(\cdot)$ is defined in (2.3), and there exists a one-to-one correspondence between l and (m,n).

Proposition 4.1. With the above setting, the FEM stiffness matrix $\boldsymbol{S}=(S_{ll'})_{1\le l,l'\le N_d}$ for

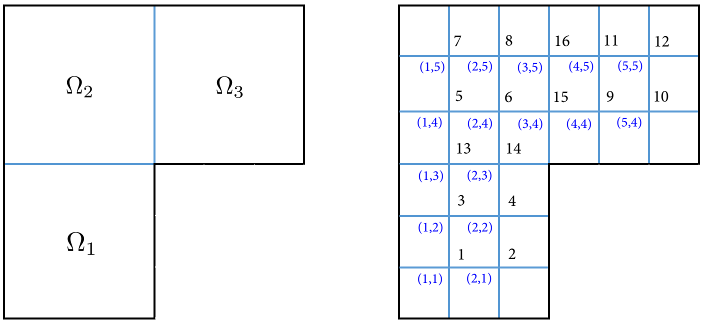

Figure 10: Illustration of an L-shaped domain Ω (left), and its partition and ordering of unknowns (right).

$s\in(0,1)$ has the form

$$\boldsymbol{S}=\widehat{C}_s\frac{h_x^{4-2s}}{h_y^2}\big(\widetilde{\boldsymbol{S}}+\widehat{\boldsymbol{S}}\big), \tag{4.6}$$

where the Toeplitz structure matrix $\widetilde{\boldsymbol{S}}$ and non-Toeplitz structure matrix $\widehat{\boldsymbol{S}}$ are given by

$$\widetilde{\boldsymbol{S}}=\begin{bmatrix} \mathbb{T}_{11} & \mathbb{T}_{12} & \mathbb{T}_{13} & \mathbb{T}_{14} & 0 \\ \mathbb{T}_{12}^t & \mathbb{T}_{11} & \mathbb{T}_{23} & \mathbb{T}_{24} & 0 \\ \mathbb{T}_{13}^t & \mathbb{T}_{23}^t & \mathbb{T}_{11} & \mathbb{T}_{34} & 0 \\ \mathbb{T}_{14}^t & \mathbb{T}_{24}^t & \mathbb{T}_{34}^t & \boldsymbol{T}_0 & 0 \\ 0 & 0 & 0 & 0 & \boldsymbol{T}_0 \end{bmatrix},\ \widehat{\boldsymbol{S}}=\begin{bmatrix} 0 & 0 & 0 & 0 & \mathbb{D}_{15} \\ 0 & 0 & 0 & 0 & \mathbb{D}_{25} \\ 0 & 0 & 0 & 0 & \mathbb{D}_{35} \\ 0 & 0 & 0 & 0 & \mathbb{D}_{45} \\ \mathbb{D}_{15}^t & \mathbb{D}_{25}^t & \mathbb{D}_{35}^t & \mathbb{D}_{45}^t & 0 \end{bmatrix}, \tag{4.7}$$

with $\mathbb{T}_{11}$, $\mathbb{T}_{12}$, $\mathbb{T}_{13}$ and $\mathbb{T}_{23}$ being $\widetilde{N}$-by-$\widetilde{N}$ block-Toeplitz matrices, $\mathbb{T}_{14}$, $\mathbb{T}_{24}$, $\mathbb{T}_{34}$ being $\widetilde{N}$-by-1 block-Toeplitz matrices, and $\mathbb{D}_{i5}$, $i=1,2,3,4$ being non-Toeplitz matrices whose representations can be referred to Appendix E. In the above, the constant $\widehat{C}_s$ is defined in (2.13), and Toeplitz matrix $\boldsymbol{T}_0$ is defined in (2.11).

In actual computations, we adopt the conjugate gradient (CG) method where the matrix-vector multiplication can be implemented efficiently as in [17] (but block by block). More precisely, we split the vector $\vec{u}$ into five parts, and evaluate the matrix-vector multiplications $\mathbb{T}_{i1}\vec{u}_1,\mathbb{T}_{i2}\vec{u}_2$, $\mathbb{T}_{i3}\vec{u}_3$, $i=1,2,3$, and $\mathbb{T}_{i4}\vec{u}_4$, $i=1,2,3,4$ one by one, which can be done carried out by using FFT (cf. [43]). The non-Toeplitz part involving $\mathbb{D}_{i5}\vec{u}_5,i=1,2,3,4$, is however of much smaller size.

Here, we first examine the convergence rate of the proposed method on (4.3) with an "exact" solution. Set $\Omega=(-1/4,3/4)\times(-3/4,1/4)\backslash[1/4,3/4]\times[-3/4,-1/4]$, $h_x=h_y=h$, and $\lambda=25$ to ensure $u_\lambda(\boldsymbol{x})$ to be nearly zero outside Ω. In this case, we expect a second-order convergence as before. We tabulate in Table 2 the numerical errors, which indicate a second-order convergence.

Table 2: Errors for the "exact" solution u_λ with $\lambda=25$ in an L-shaped domain.

h	$s=0.3$				$s=0.7$			
	L^∞-error	Order	L^2-error	Order	L^∞-error	Order	L^2-error	Order
2^{-5}	6.78e-2	–	9.60e-3	–	5.38e-2	–	7.70e-3	–
2^{-6}	2.21e-2	1.61	2.46e-3	1.96	1.90e-2	1.50	2.13e-3	1.85
2^{-7}	6.03e-3	1.87	6.26e-4	1.97	5.44e-3	1.80	5.68e-4	1.92
2^{-8}	1.55e-3	1.95	1.58e-4	1.98	1.45e-3	1.90	1.44e-4	1.93
2^{-9}	3.93e-4	1.97	3.98e-5	1.98	3.75e-4	1.95	3.90e-5	1.88

We next test the scheme upon (1.3) with $f(x)=1$. We illustrate the profiles of the numerical solutions obtained by the FEM scheme with $M=N=1024$ in Fig. 11, which clearly exhibits the boundary and corner singularities. In Fig. 12, we plot the L^∞- and L^2-errors in log-log scale against various h with the reference order of convergence, which, to the best of our knowledge, has not been reported in the literature.

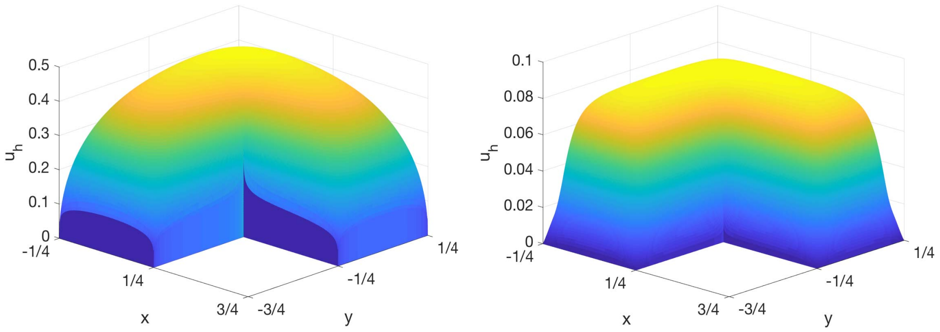

Figure 11: Profile of u_h with $M=N=1024$. Left: $s=0.3$. Right: $s=0.7$.

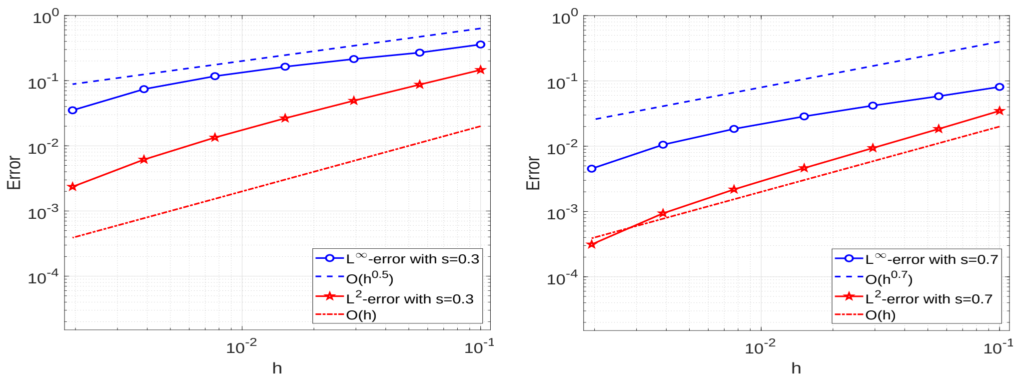

Figure 12: The errors for $f(x)=1$. Left: $s=0.3$. Right: $s=0.7$.

4.3 Applications to the fractional-in-space Allen-Cahn equation

Consider the fractional-in-space Allen-Cahn equation of the form

$$\begin{cases} u_t(\boldsymbol{x},t)+\epsilon^2(-\Delta)^s u(\boldsymbol{x},t)+f(u(\boldsymbol{x},t))=0, & \text{in } \Omega\times(0,T], \\ u(\boldsymbol{x},t)=0, & \text{in } \Omega^c\times[0,T], \\ u(\boldsymbol{x},0)=u_0(\boldsymbol{x}), & \text{in } \bar{\Omega}, \end{cases} \tag{4.8}$$

for $s\in(0,1)$, and $\epsilon>0$, where

$$f(u)=F'(u)=\frac{u(u-1)(2u-1)}{2} \text{ with } F(u)=\frac{u^2(u-1)^2}{4}.$$

Let u_h^k be the FEM approximation of u at time $t_k=k\tau$. Using the semi-implicit Euler discretization in time and FEM in space, we derive the fully discretised scheme for (4.8) is to find $u_h^{k+1}\in\mathbb{V}_h$ such that

$$\frac{1}{\tau}\big(u_h^{k+1}-u_h^k,v_h\big)_\Omega+\epsilon^2\big((-\Delta)^s u_h^{k+1},v_h\big)_\Omega+\big(f(u_h^k),v_h\big)_\Omega=0,\ \forall v_h\in\mathbb{V}_h. \tag{4.9}$$

We refer to [30] for more details of such time-stepping schemes for gradient flows. Then the corresponding matrix form reads

$$\big(\boldsymbol{M}+\tau\epsilon^2\boldsymbol{S}\big)\,U^{k+1}=\boldsymbol{M}U^k-\tau F^k, \tag{4.10}$$

where $\boldsymbol{S}$ is the stiffness matrix defined in (2.10), and

$$\begin{aligned} &U^k=\big(\tilde{u}_{11}^k,\tilde{u}_{21}^k,\cdots,\tilde{u}_{M1}^k,\tilde{u}_{12}^k,\tilde{u}_{22}^k,\cdots,\tilde{u}_{M2}^k,\cdots\cdots,\tilde{u}_{1N}^k,\tilde{u}_{2N}^k,\cdots,\tilde{u}_{MN}^k\big)^t\in\mathbb{R}^{MN}, \\ &\boldsymbol{M}=(M_{ll'})_{1\le l,l'\le MN}, \quad M_{ll'}=\int_\Omega \phi_m(x)\phi_n(y)\phi_{m'}(x)\phi_{n'}(y)\,\mathrm{d}x\mathrm{d}y, \end{aligned}$$

with $l=(n-1)M+m$ and $1\le l\le MN$. Likewise for F^k, but with the components $f_{mn}^k=(f(u_n^k),\phi_m\phi_n)_\Omega$.

4.3.1 Accuracy test

We first test the convergence rate of the full discrete scheme (4.9). For this purpose, we consider (4.8) with an exact solution by adding an extra right hand side g, that is,

$$u_t(\boldsymbol{x},t)+\epsilon^2(-\Delta)^s u(\boldsymbol{x},t)+f(u(\boldsymbol{x},t))=g(\boldsymbol{x},t) \text{ in } \Omega\times(0,T].$$

We choose $u(\boldsymbol{x},t)=\mathrm{e}^{-t-\lambda^2\|\boldsymbol{x}\|^2/2}$, and find from (4.3) that

$$\begin{aligned} g(\boldsymbol{x},t)=&\,2^s\lambda^{2s}\Gamma(s+1)\epsilon^2\mathrm{e}^{-t}\,{}_1F_1(s+1,1,-\lambda^2\|\boldsymbol{x}\|^2/2) \\ &-\frac{1}{2}\mathrm{e}^{-t-\lambda^2\|\boldsymbol{x}\|^2/2}-\frac{3}{2}\mathrm{e}^{-2t-\lambda^2\|\boldsymbol{x}\|^2}+\mathrm{e}^{-3t-3\lambda^2\|\boldsymbol{x}\|^2/2}. \end{aligned}$$

We take $\epsilon=0.1$, $L=1$, $T=1$, $\lambda=12$, and $s=0.7$. To show the convergence of spatial discretization, we set the time step $\tau=10^{-5}$ so that the time discretization error is negligible. We tabulate the spatial maximum errors on the left side of Table 3. To illustrate the temporal error, we choose the mesh size $h=2^{-9}$ so that the temporal error dominates. We list the temporal maximum errors on the right side of Table 3. We can observe that spatial error is of order $O(h^2)$, while the temporal error is of order $O(\tau)$.

Table 3: Errors and convergence rates with respect to (h,τ).

	Spatial convergence			Temporal convergence	
h	Errors	c.r.	τ	Errors	c.r.
2^{-4}	8.67e-2	–	1/5	6.55e-2	–
2^{-5}	2.87e-2	1.59	1/10	3.42e-2	0.93
2^{-6}	8.02e-3	1.84	1/20	1.75e-2	0.96
2^{-7}	1.42e-3	2.49	1/40	8.84e-3	0.98
2^{-8}	3.18e-4	2.13	1/80	4.43e-3	0.99
2^{-9}	7.36e-5	2.11	1/160	2.21e-3	1.00

4.3.2 Phase separation and interfacial width

We take $\Omega=(-2,2)^2$, $\epsilon=0.01$, $\tau=10^{-4}$, $M=N=2^{10}$ and the initial data $u_0(\boldsymbol{x})=\frac{4}{5}\mathrm{e}^{-\|\boldsymbol{x}\|^2}$. In Fig. 13, we plot the snapshots of the solution at $t=0,4,8,12$ with $s=0.7$. We observe a clear phase separation and see that the interface becomes sharper as time evolves.

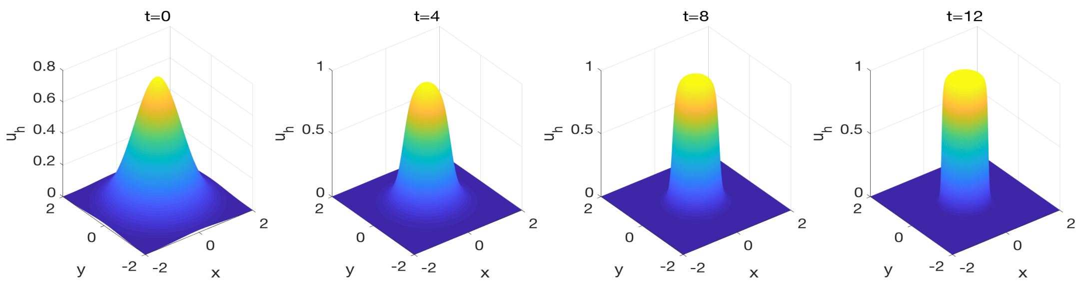

Figure 13: The evolution of solution using semi-implicit scheme at $t=0,4,8,12$ with $s=0.7$.

The interfacial width of the fractional-in-space Allen-Cahn equation has been studied numerically in one dimensional case (cf. [16, 32, 37, 39]), and the predicted interfacial is of the order $O(\epsilon^{1/s})$. We also refer to [2] for some interesting analysis on the asymptotic behavior of the interfacial width and free energy functional as $s\to 0$, which leads to the displacement of the equilibrium states. It is therefore of interest to see what happens to the two-dimensional case. Here, we measure the width of the interface through a profile along the x-axis with the threshold $0.01<u(x,0)<0.99$, i.e., the length of the interval

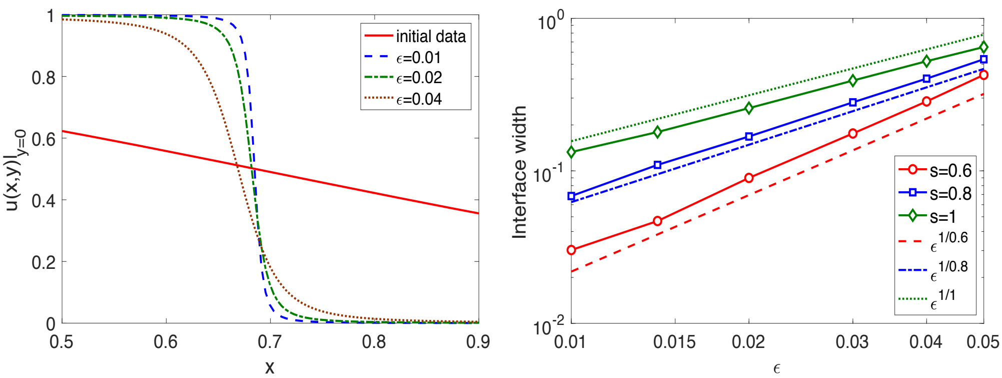

Figure 14: Left: Interfacial layer against various ϵ with $s=0.7$ zoomed in $[0.5,0.9]$ at $T=20$. Right: Interfacial width against various ϵ and s at $T=20$.

$\{x : 0.01 < u(x,0) < 0.99, x \in [0,2]\}$. For this purpose, we consider the fractional order $s=0.7$ and take $T=20$, $\tau=10^{-2}$, and $M=N=2^{10}$. We plot in Fig. 14 (left) the interfacial region at $y=0$ and within a small interval of x, for several values of ϵ. We see that the interfacial layer becomes sharper as ϵ decreases. In Fig. 14 (right), we plot the interfacial width against ϵ with various s, which indicates a behaviour of $O(\epsilon^{1/s})$ as with the one-dimensional case.

Finally, we adopt the scheme to simulate (4.8) with two "kissing" bubbles. The initial value is chosen as the two "kissing" bubbles of the form

$$u_0(\boldsymbol{x}) = 1 - \frac{1}{2}\tanh\Big(\frac{d(\boldsymbol{x},\boldsymbol{x}_1)}{\delta}\Big) - \frac{1}{2}\tanh\Big(\frac{d(\boldsymbol{x},\boldsymbol{x}_2)}{\delta}\Big), \tag{4.11}$$

where $\delta > 0$, the function $d(\boldsymbol{x},\boldsymbol{x}_i) = |\boldsymbol{x}-\boldsymbol{x}_i| - 0.27$, and the two bubbles are initially centered at $\boldsymbol{x}_1 = (-0.2,-0.2)$ and $\boldsymbol{x}_2 = (0.2,0.2)$. Here $\Omega = (-1,1)^2$, $\delta = 0.03$, $\epsilon = 0.01$, $M=N=2^{10}$, and the time step $\tau = 0.0002$. In Fig. 15, we plot the time evolution of the two bubbles for different $s = 0.3,0.7,0.9$. At $t=1$, the two bubbles are connected with each other, and then coalesce into one bubble as time goes on. We observe indeed from each column of Fig. 15 that the coalescence of the two bubbles become much faster as s increases, i.e., the dynamics evolves faster for a bigger fractional power s.

5 Concluding remarks and discussions

In this paper, we showed that the entries of the FEM stiffness matrix, associated with the IFL with global homogeneous boundary conditions on rectangular meshes, could be explicitly represented as one-dimensional integrals on a finite interval. Then we developed an efficient algorithm for computing the one-dimensional integral based on the binomial expansion and Jacobi-Gauss quadrature for dealing with the boundary and interior singularities, respectively. This allowed for the computation of the entries accurately within any controllable accuracy, and enabled us to study the decay rate the entries that led

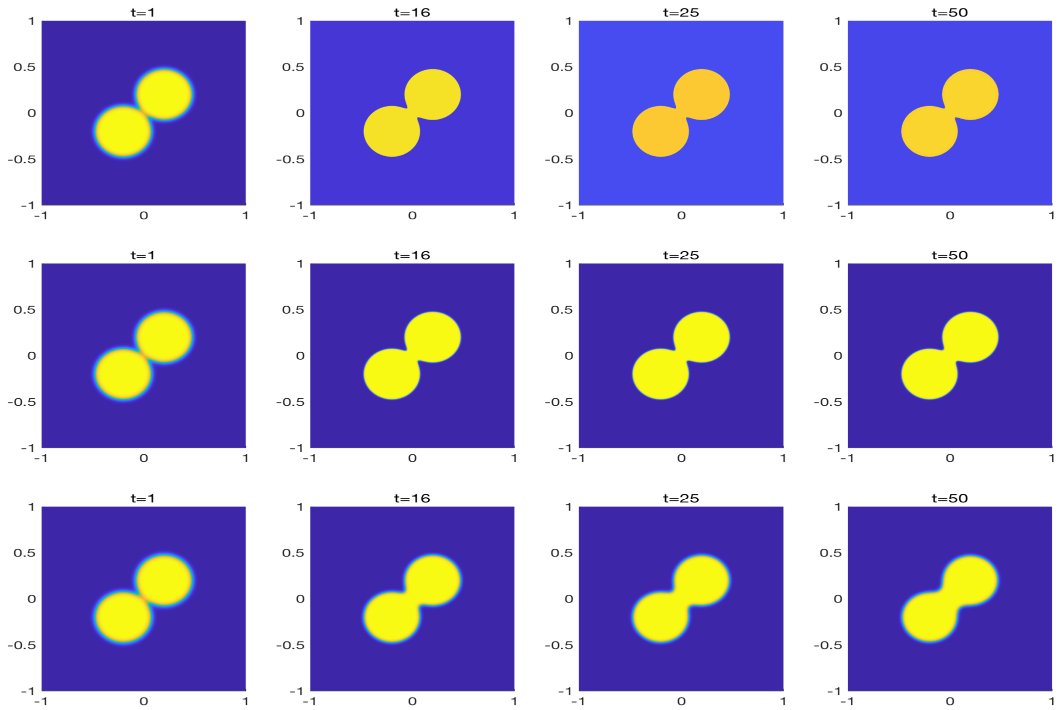

Figure 15: Time evolution of two "kissing" bubbles. Top: $s=0.3$. Middle: $s=0.7$. Bottom: $s=0.9$.

to substantial saving in computational cost. As an application, we introduced a semi-implicit scheme for solving the fractional-in-space Allen-Cahn equation. Our numerical experiments demonstrated that our algorithms are efficient and accurate.

Finally, we demonstrate the idea of dealing with the fractional Poisson equation with nonhomogeneous Dirichlet boundary conditions. To this end, let $u(\boldsymbol{x})$ be a function defined on $\mathbb{R}^2$ and denote its restriction on the finite domain Ω by $u_\Omega(\boldsymbol{x})=u(\boldsymbol{x})|_{\boldsymbol{x}\in\Omega}$. Given $g(\boldsymbol{x})$ defined on Ω^c, we look for

$$u(\boldsymbol{x})=\begin{cases} u_\Omega(\boldsymbol{x}), & \boldsymbol{x}\in\Omega, \\ g(\boldsymbol{x}), & \boldsymbol{x}\in\Omega^c, \end{cases} \quad \text{i.e., the unknown } u_\Omega(\boldsymbol{x}), \tag{5.1}$$

such that

$$(-\Delta)^s u(\boldsymbol{x})=f(\boldsymbol{x}) \ \text{ in } \Omega. \tag{5.2}$$

It is clear that we can write the solution as

$$u(\boldsymbol{x})=\tilde{u}_\Omega(\boldsymbol{x})+\tilde{g}(\boldsymbol{x}), \quad \boldsymbol{x}\in\mathbb{R}^2,$$

where $\tilde{u}_\Omega$ (resp. $\tilde{g}$) is the zero extension of u_Ω (resp. g) on Ω (resp. Ω^c) to $\mathbb{R}^2$. Then the problem of interest becomes

$$(-\Delta)^s\tilde{u}_\Omega(\boldsymbol{x})=f(\boldsymbol{x})-(-\Delta)^s\tilde{g}(\boldsymbol{x}). \tag{5.3}$$

Thus our proposed approach can be applied with extra cost for evaluating $(-\Delta)^s\tilde{g}(\boldsymbol{x})$ at the FEM grids. In practice, we can use a suitable approximation of $\tilde{g}(\boldsymbol{x})$ so that its fractional Laplacian can be computed efficiently or ideally explicitly. For example, a good candidate is the radial basis approximation, since the fractional Laplacian of such a basis can be expressed in terms of hypergeometric functions (cf. [15, (2.4)]).

Appendix A: Proof of Proposition 3.1

Recall the basic binomial expansion: if $|A|<|B|$ and $B\neq 0$. Then we have

$$|A-B|^\gamma+|A+B|^\gamma=|B|^\gamma\Big(1-\frac{A}{B}\Big)^\gamma+|B|^\gamma\Big(1+\frac{A}{B}\Big)^\gamma=2|B|^\gamma\sum_{n=0}^{\infty}\frac{(\gamma)_{2n}}{(2n)!}\Big(\frac{A}{B}\Big)^{2n}. \tag{A.4}$$

Taking $A=x_{j+p}\sin\theta$ and $B=y_{k+q}\cos\theta$ in (A.4), we obtain immediately that if $\tan\theta<\tan\vartheta_{j+p}^{k+q}$ for all $p\in\Upsilon_j, q\in\Upsilon_k$ in (3.2), then

$$\begin{aligned}
&\big|x_{j+p}\sin\theta-y_{k+q}\cos\theta\big|^\gamma+\big|x_{j+p}\sin\theta+y_{k+q}\cos\theta\big|^\gamma\\
&=2|B|^\gamma\sum_{n=0}^{\infty}\frac{(\gamma)_{2n}}{(2n)!}\Big(\frac{A}{B}\Big)^{2n}=2(y_{k+q}\cos\theta)^\gamma\sum_{n=0}^{\infty}\frac{(\gamma)_{2n}}{(2n)!}\Big(\frac{x_{j+p}\sin\theta}{y_{k+q}\cos\theta}\Big)^{2n}\\
&=2(\bar{y}_{k+q}\mathcal{C}_k(\theta))^\gamma\sum_{n=0}^{\infty}\frac{(\gamma)_{2n}}{(2n)!}\Big(\frac{\bar{x}_{j+p}}{\bar{y}_{k+q}}\Big)^{2n}\Big(\frac{\mathcal{S}_j(\theta)}{\mathcal{C}_k(\theta)}\Big)^{2n}.
\end{aligned} \tag{A.5}$$

If $k\geq 3$, then $y_{k+q}>0$, then we derive from (2.30) and (A.5) that

$$F_j^k(\theta)=\frac{2x_{j+2}^4y_{k+2}^4}{h^\gamma}\sum_{n=0}^{\infty}\frac{(\gamma)_{2n}\bar{C}_{2n}^{j,k}}{(2n)!}\frac{(\mathcal{S}_j(\theta))^{2n-4}}{(\mathcal{C}_k(\theta))^{2n-2+2s}}, \tag{A.6}$$

where the constant

$$\bar{C}_{2n}^{j,k}=\sum_{p,q=-2}^{2}c_pc_q\bar{y}_{k+q}^{\gamma}\Big(\frac{\bar{x}_{j+p}}{\bar{y}_{k+q}}\Big)^{2n}=\Big(\sum_{|p|=0}^{2}c_p\bar{x}_{j+p}^{2n}\Big)\Big(\sum_{|q|=0}^{2}c_q\bar{y}_{k+q}^{\gamma-2n}\Big). \tag{A.7}$$

Given $\{c_p\}$ in (2.13), we find readily that for $m=0,1,2,3$,

$$\sum_{|p|=0}^{2}c_p\bar{x}_{j+p}^m=\frac{1}{(j+2)^m}\sum_{|p|=0}^{2}c_p(j+p)^m=0, \tag{A.8}$$

but for $m=4$, it does not vanish. Then using the substitution: $n\to n-2$ and denoting $C_{2n}^{j,k}=\bar{C}_{2n+4}^{j,k}$, we integrate both sides of the resulted equation over $(0,\vartheta)$ and obtain (3.8) with $j\geq k\geq 3$.

If $k=0,1,2$, then for $q=-k$, $y_{k+q}=0$, so the corresponding term at the left-hand side of (A.5) can be kept intact. Accordingly, we have

$$\begin{aligned} F_j^k(\theta) &= \frac{h^{-\gamma}}{\sin^4\theta\cos^4\theta}\sum_{|p|=0}^{2} c_p\Big\{2c_{-k}\big(x_{j+p}\sin\theta\big)^{\gamma} \\ &\quad + \sum_{|q|=0;q\neq -k}^{2}\big(|x_{j+p}\sin\theta - y_{k+q}\cos\theta|^{\gamma} + |x_{j+p}\sin\theta + y_{k+q}\cos\theta|^{\gamma}\big)\Big\} \qquad \text{(A.9)} \\ &= \frac{2x_{j+2}^4 y_{k+2}^4}{h^{\gamma}}\Big\{\widetilde{C}^{j,k}\frac{(\mathcal{S}_j(\theta))^{2-2s}}{(\mathcal{C}_k(\theta))^4} + \sum_{n=0}^{\infty}\frac{(\gamma)_{2n}\tilde{C}_{2n}^{j,k}}{(2n)!}\frac{(\mathcal{S}_j(\theta))^{2n-4}}{(\mathcal{C}_k(\theta))^{2n-2+2s}}\Big\}, \end{aligned}$$

where $\tilde{C}_{2n}^{j,k}$ is the same as $\bar{C}_{2n}^{j,k}$ in (A.7) but excluding the term $q=-k$ in the summation $\sum_{|q|=0}^{2}$. In view of (A.8), we have $\tilde{C}_0^{j,k}=\tilde{C}_2^{j,k}=0$, so with a change of index $n\to n-2$, denoting $C_{2n}^{j,k}=\tilde{C}_{2n+4}^{j,k}$, and integrating both sides over $(0,\vartheta)$, we can obtain (3.8) with $0\le k\le 2$ similarly.

Next, we turn to prove (3.10). Recall the formulas (cf. [26, P. 152]): for any $\mu,\nu\in\mathbb{R}$ and $\nu\neq 1$,

$$\int\frac{\sin^{\mu}\theta}{\cos^{\nu}\theta}\,\mathrm{d}\theta = \frac{\sin^{\mu-1}\theta}{(\nu-1)\cos^{\nu-1}\theta} - \frac{\mu-1}{\nu-1}\int\frac{\sin^{\mu-2}\theta}{\cos^{\nu-2}\theta}\,\mathrm{d}\theta \qquad \text{(A.10a)}$$

$$= \frac{\sin^{\mu+1}\theta}{(\nu-1)\cos^{\nu-1}\theta} - \frac{\mu-\nu+2}{\nu-1}\int\frac{\sin^{\mu}\theta}{\cos^{\nu-2}\theta}\,\mathrm{d}\theta. \qquad \text{(A.10b)}$$

Taking $\mu=2n$ and $\nu=2n+2+2s$ in (A.10a), we obtain (3.10) from the resulted recurrence relation and (3.6) straightforwardly.

Finally, we prove (3.11). Using (A.10b) with $\mu=2-2s,\nu=4$ and $\mu=2-2s,\nu=2$ consecutively, yields

$$\int_0^{\vartheta}\frac{(\sin\theta)^{2-2s}}{(\cos\theta)^4}\,\mathrm{d}\theta = \frac{(\sin\vartheta)^{3-2s}}{3(\cos\vartheta)^3} + \frac{2s(\sin\vartheta)^{3-2s}}{3\cos\vartheta} + \frac{4s(s-1)}{3}\int_0^{\vartheta}(\sin\theta)^{2-2s}\,\mathrm{d}\theta.$$

With the variable substitution $t=\sin^2\theta$, we find that

$$\int_0^{\vartheta}(\sin\theta)^{2-2s}\,\mathrm{d}\theta = \frac{1}{2}\int_0^{\sin^2\vartheta} t^{\frac{1}{2}-s}(1-t)^{-\frac{1}{2}}\,\mathrm{d}t = \frac{1}{2}B(\sin^2\vartheta;3/2-s,1/2). \qquad \text{(A.11)}$$

Thus, the identity (3.11) follows.

Appendix B: Proof of Proposition 3.2

Let $\widetilde{F}_j^k(\theta)$ be the first N_δ-term truncation of (A.9) that gives the integrand of $\widetilde{\mathcal{I}}_j^k(\theta)$ in (3.13). Thus, we have

$$\begin{aligned}
F_j^k(\theta)-\widetilde{F}_j^k(\theta) &= \frac{2x_{j+2}^4 y_{k+2}^4}{h^\gamma}\sum_{n=N_\delta}^{\infty}\frac{(\gamma)_{2n+4}C_{2n}^{j,k}}{(2n+4)!}\frac{(\mathcal{S}_j(\theta))^{2n}}{(\mathcal{C}_k(\theta))^{2n+2+2s}}\\
&=\frac{2}{h^\gamma}\sum_{n=N_\delta}^{\infty}\frac{(\gamma)_{2n+4}}{(2n+4)!}\left(\sum_{|p|=0}^{2}c_p x_{j+p}^{2n+4}\right)\left(\sum_{q\in\Upsilon_k}c_q y_{k+q}^{2-2n-2s}\right)\frac{(\sin\theta)^{2n}}{(\cos\theta)^{2n+2+2s}}\\
&=\frac{2}{h^\gamma(\cos\theta)^{2+2s}}\sum_{n=N_\delta}^{\infty}\frac{(\gamma)_{2n+4}}{(2n+4)!}\left(\sum_{|p|=0}^{2}c_p x_{j+p}^4\sum_{q\in\Upsilon_k}c_q y_{k+q}^{2-2s}\frac{(x_{j+p}\sin\theta)^{2n}}{(y_{k+q}\cos\theta)^{2n}}\right),
\end{aligned}$$

where we substituted $\mathcal{S}_j(\theta)=x_{j+2}\sin\theta, \mathcal{C}_k(\theta)=y_{k+2}\cos\theta$ (cf. (3.6)) and $C_{2n}^{j,k}$ in (3.7) into the above. Under the condition (3.14), we can obtain the bound

$$\begin{aligned}
\left|F_j^k(\theta)-\widetilde{F}_j^k(\theta)\right| &\le \frac{2}{h^\gamma(\cos\theta)^{2+2s}}\sum_{|p|=0}^{2}|c_p|x_{j+p}^4\sum_{q\in\Upsilon_k}|c_q|y_{k+q}^{2-2s}\sum_{n=N_\delta}^{\infty}\frac{|(\gamma)_{2n+4}|\delta^{2n}}{(2n+4)!}\\
&\le \frac{2}{(\cos\theta)^{2+2s}}\sum_{|p|=0}^{2}|c_p||j+p|^4\sum_{q\in\Upsilon_k}|c_q||k+q|^{2-2s}\sum_{n=N_\delta}^{\infty}\frac{|(\gamma)_{2n+4}|\delta^{2n}}{(2n+4)!}.
\end{aligned}$$

Using (2.25) with $z=2n-2+2s$, we can rewrite the falling factorial as

$$(\gamma)_{2n+4}=(6-2s)_{2n+4}=\frac{\Gamma(7-2s)}{\Gamma(3-2n-2s)}=\pi^{-1}\Gamma(7-2s)\Gamma(2n+2s-2)\sin(2s\pi).$$

Using the Stirling's formula, we obtain

$$\begin{aligned}
\sum_{n=N_\delta}^{\infty}\frac{|(\gamma)_{2n+4}|\delta^{2n}}{(2n+4)!} &= \frac{\Gamma(7-2s)|\sin(2s\pi)|}{\pi}\sum_{n=N_\delta}^{\infty}\frac{\Gamma(2n+2s-2)\delta^{2n}}{\Gamma(2n+5)}\\
&\le \frac{c\Gamma(7-2s)|\sin(2s\pi)|}{\pi}\sum_{n=N_\delta}^{\infty}\frac{\delta^{2n}}{(2n)^{7-2s}} \le \frac{c\Gamma(7-2s)|\sin(2s\pi)|}{\pi}\int_{N_\delta}^{\infty}\frac{\delta^{2x}}{(2x)^{7-2s}}\mathrm{d}x\\
&\le \frac{c\Gamma(7-2s)|\sin(2s\pi)|}{\pi|\ln\delta|}\frac{\mathrm{e}^{(2\ln\delta)N_\delta}}{(2N_\delta)^{7-2s}},
\end{aligned}$$

where the constant from $c\approx 1$. Therefore, we can bound the truncation error

$$\left|\mathcal{I}_j^k(\vartheta)-\widetilde{\mathcal{I}}_j^k(\vartheta)\right| \le \int_0^{\vartheta}|F_j^k(\theta)-\widetilde{F}_j^k(\theta)|\mathrm{d}\theta$$

from the above estimates.

Appendix C: Proof of Proposition 3.3

We obtain from (2.30), (3.4) and the fundamental trigonometric identity that

$$
\begin{aligned}
\mathcal{J}_j^k(\theta_1,\theta_2) &= \int_{\theta_1}^{\theta_2} \frac{h^{-\gamma}}{\sin^4\theta\cos^4\theta} \sum_{p,q=-2}^{2} c_p c_q \Big\{ \big|x_{j+p}\sin\theta - y_{k+q}\cos\theta\big|^{\gamma} + \big|x_{j+p}\sin\theta + y_{k+q}\cos\theta\big|^{\gamma} \Big\} \mathrm{d}\theta \\
&= \frac{1}{h^{\gamma}} \sum_{p,q=-2}^{2} c_p c_q (x_{j+p}^2 + y_{k+q}^2)^{\frac{\gamma}{2}} \mathcal{I}_{p,q},
\end{aligned}
\tag{C.12}
$$

where

$$
\mathcal{I}_{p,q} := \int_{\theta_1}^{\theta_2} \frac{|\sin(\theta - \vartheta_p^q)|^{\gamma}}{\sin^4\theta\cos^4\theta} \mathrm{d}\theta + \int_{\theta_1}^{\theta_2} \frac{|\sin(\theta + \vartheta_p^q)|^{\gamma}}{\sin^4\theta\cos^4(\theta)} \mathrm{d}\theta. \tag{C.13}
$$

We can always assume that $x_{j+p}^2 + y_{k+q}^2 \neq 0$, as the contribution of the term in (C.12) is zero when $x_{j+p}^2 + y_{k+q}^2 = 0$. Then, we only need to consider the following two cases to carry out the proof.

(i) $x_{j+p} = 0$ **or** $y_{k+q} = 0$**:** If $y_{k+q} = 0$, i.e., $q = -k$ ($k = 0,1,2$) and $\vartheta_p^q = 0$, then we find from (C.13) and (3.9) that

$$
\mathcal{I}_{p,q} = 2\int_{\theta_1}^{\theta_2} \frac{\sin^{\gamma}\theta}{\sin^4\theta\cos^4\theta} \mathrm{d}\theta = \frac{2y_{k+2}^4}{x_{j+2}^{2-2s}} \int_{\theta_1}^{\theta_2} \frac{(\mathcal{S}_j(\theta))^{2-2s}}{(\mathcal{C}_k(\theta))^4} \mathrm{d}\theta = \frac{2y_{k+2}^4}{x_{j+2}^{2-2s}} \big(\widetilde{R}(\theta_2) - \widetilde{R}(\theta_1)\big). \tag{C.14}
$$

Similarly, if $x_{j+p} = 0$, i.e., $p = -j$ ($j = 0,1,2$) and $\vartheta_p^q = \frac{\pi}{2}$, then

$$
\mathcal{I}_{p,q} = 2\int_{\theta_1}^{\theta_2} \frac{\cos^{\gamma}\theta}{\sin^4\theta\cos^4\theta} \mathrm{d}\theta = \frac{2x_{j+2}^4}{y_{k+2}^{2-2s}} \int_{\theta_1}^{\theta_2} \frac{(\mathcal{C}_k(\theta))^{2-2s}}{(\mathcal{S}_j(\theta))^4} \mathrm{d}\theta = \frac{2y_{k+2}^4}{x_{j+2}^{2-2s}} \big(\widetilde{R}(\pi/2 - \theta_2) - \widetilde{R}(\pi/2 - \theta_1)\big). \tag{C.15}
$$

(ii) $x_{j+p} \neq 0$ **and** $y_{k+q} \neq 0$**:** In this case, we have $0 < \theta_1 \le \vartheta_p^q \le \theta_2 < \frac{\pi}{2}$. It is evident that the first integrand of (C.13) is singular at $\theta = \vartheta_p^q$, while that of the second integrand is regular. We only deal with the former, and split it into

$$
\begin{aligned}
\int_{\theta_1}^{\theta_2} \frac{|\sin(\theta - \vartheta_p^q)|^{\gamma}}{\sin^4\theta\cos^4\theta} \mathrm{d}\theta &= 16\int_{\theta_1}^{\vartheta_p^q} \frac{(\sin(\vartheta_p^q - \theta))^{\gamma}}{\sin^4(2\theta)} \mathrm{d}\theta + 16\int_{\vartheta_p^q}^{\theta_2} \frac{(\sin(\theta - \vartheta_p^q))^{\gamma}}{\sin^4(2\theta)} \mathrm{d}\theta \\
&= 16\int_{-1}^{1} \left\{ \frac{\sin(d_1(1+z))}{d_1(1+z)} \right\}^{\gamma} \frac{d_1^{\gamma+1}(1+z)^5}{\sin^4(2w_1(z))} (1+z)^{1-2s} \mathrm{d}z \\
&\quad + 16\int_{-1}^{1} \left\{ \frac{\sin(d_2(1+z))}{d_2(1+z)} \right\}^{\gamma} \frac{d_2^{\gamma+1}(1+z)^5}{\sin^4(2w_2(z))} (1+z)^{1-2s} \mathrm{d}z,
\end{aligned}
\tag{C.16}
$$

where we used the variable substitutions $\theta = w_1(z)$ and $\theta = w_2(z)$ in the second identity, and d_1, d_2 are defined in (3.17). This ends the proof.

Appendix D: Proof of Proposition 3.4

Our starting point is to show that if

$$(j+p)\cos\theta+(k+q)\sin\theta\neq 0, \quad \text{i.e.,} \quad \theta\neq -\arctan\Big(\frac{j+p}{k+q}\Big), \tag{D.17}$$

for $p,q\in\{\pm 2,\pm 1,0\}$ and $j\ge k\ge 0$, but $j^2+k^2\neq 0$, then the function $f_j^k(\theta)$ in (2.12) satisfies

$$f_j^k(\theta)=\frac{(6-2s)_8}{|j\cos\theta+k\sin\theta|^{2+2s}}\bigg\{1+\frac{(1+s)(3+2s)}{3(j\cos\theta+k\sin\theta)^2}+O(h^4)\bigg\}. \tag{D.18}$$

Recall the finite difference formula derived from the Taylor formula:

$$\begin{aligned}{}^c\mathcal{D}_x^4[v](x)&:=\sum_{p=-2}^{2}c_p v(x+ph)=v(x-2h)-4v(x-h)+6v(x)-4v(x+h)+v(x+2h)\\ &=h^4v^{(4)}(x)+\frac{h^6}{6}v^{(6)}(x)+\frac{h^8}{80}v^{(8)}(x)+\sum_{k=5}^{\infty}\frac{(2^{2k+1}-8)h^{2k}}{(2k)!}v^{(2k)}(x),\end{aligned} \tag{D.19}$$

where we assume that all derivatives of v at x exist. In view of (2.12), we define the function

$$U(x,y):=U(x,y;\theta)=\big|x\cos\theta+y\sin\theta\big|^{\gamma}, \tag{D.20}$$

where $\theta\in(-\pi/2,\pi/2)$ can be viewed as a parameter. We further introduce a set of "virtual" grids

$$X_j=jh,\ Y_k=kh, \quad -2\le j\le J+2,\ -2\le k\le K+2.$$

Then, we find from (2.12) and (D.20) that

$$f_j^k(\theta)=\frac{h^{-\gamma}}{\sin^4\theta\cos^4\theta}\,{}^c\mathcal{D}_y^4\circ{}^c\mathcal{D}_x^4[U](X_j,Y_k), \quad j,k\ge 0. \tag{D.21}$$

Thus, using (D.21) and (D.19), we have that for $j^2+k^2\neq 0$

$$\begin{aligned}f_j^k(\theta)&=\frac{h^{2s-2}}{\sin^4\theta\cos^4\theta}\sum_{q=-2}^{2}c_q\Big\{\partial_x^4U(X_j,Y_{k+q})+\frac{h^2}{6}\partial_x^6U(X_j,Y_{k+q})+O(h^4)\Big\}\\ &=\frac{h^{2+2s}}{\sin^4\theta\cos^4\theta}\Big\{\partial_x^4\partial_y^4U(X_j,Y_k)+\frac{h^2}{6}\partial_x^6\partial_y^4U(X_j,Y_k)+\frac{h^2}{6}\partial_x^4\partial_y^6U(X_j,Y_k)+O(h^4)\Big\}.\end{aligned} \tag{D.22}$$

Direct calculation from (D.20) leads to

$$\partial_x^{2n}\partial_y^{2m}U(x,y)=(6-2s)_{2n+2m}\sin^{2m}\theta\cos^{2n}\theta\,\big|x\cos\theta+y\sin\theta\big|^{\gamma-2n-2m}.$$

Then the representation (D.18) can be derived from (D.22) directly.

It is seen from (D.19) that the dependence of the integrand on j^2+k^2, where we can write

$$j\cos\theta+k\sin\theta=\sqrt{j^2+k^2}\cos(\theta-\theta^*_{jk}),\quad \theta^*_{jk}=\arctan(k/j).$$

Thus, we can extract the leading asymptotic order in Proposition 3.4.

Appendix E: The related matrices in Proposition 4.1

For the part with Toeplitz-structure $\widetilde{\boldsymbol{S}}$, the $\widetilde{N}$-by-$\widetilde{N}$ block-Toeplitz matrices $\mathbb{T}_{11}$, $\mathbb{T}_{12}$, $\mathbb{T}_{13}$ and $\mathbb{T}_{23}$ are given by

$$\mathbb{T}_{11}=\begin{bmatrix} \boldsymbol{T}_0 & \boldsymbol{T}_1 & \cdots & \boldsymbol{T}_{\widetilde{N}-2} & \boldsymbol{T}_{\widetilde{N}-1} \\ \boldsymbol{T}_1 & \boldsymbol{T}_0 & \ddots & \ddots & \boldsymbol{T}_{\widetilde{N}-2} \\ \vdots & \ddots & \ddots & \ddots & \vdots \\ \boldsymbol{T}_{\widetilde{N}-2} & \ddots & \ddots & \boldsymbol{T}_0 & \boldsymbol{T}_1 \\ \boldsymbol{T}_{\widetilde{N}-1} & \boldsymbol{T}_{\widetilde{N}-2} & \cdots & \boldsymbol{T}_1 & \boldsymbol{T}_0 \end{bmatrix},\ \mathbb{T}_{12}=\begin{bmatrix} \boldsymbol{T}_{\widetilde{N}+1} & \boldsymbol{T}_{\widetilde{N}+2} & \cdots & \boldsymbol{T}_{2\widetilde{N}-1} & \boldsymbol{T}_{2\widetilde{N}} \\ \boldsymbol{T}_{\widetilde{N}} & \boldsymbol{T}_{\widetilde{N}+1} & \ddots & \ddots & \boldsymbol{T}_{2\widetilde{N}-1} \\ \vdots & \ddots & \ddots & \ddots & \vdots \\ \boldsymbol{T}_3 & \ddots & \ddots & \boldsymbol{T}_{\widetilde{N}+1} & \boldsymbol{T}_{\widetilde{N}+2} \\ \boldsymbol{T}_2 & \boldsymbol{T}_3 & \cdots & \boldsymbol{T}_{\widetilde{N}} & \boldsymbol{T}_{\widetilde{N}+1} \end{bmatrix},$$

and

$$\mathbb{T}_{13}=\begin{bmatrix} \widetilde{\boldsymbol{T}}_{\widetilde{N}+1} & \widetilde{\boldsymbol{T}}_{\widetilde{N}+2} & \cdots & \widetilde{\boldsymbol{T}}_{2\widetilde{N}-1} & \widetilde{\boldsymbol{T}}_{2\widetilde{N}} \\ \widetilde{\boldsymbol{T}}_{\widetilde{N}} & \widetilde{\boldsymbol{T}}_{\widetilde{N}+1} & \cdots & \ddots & \widetilde{\boldsymbol{T}}_{2\widetilde{N}-1} \\ \vdots & \ddots & \ddots & \ddots & \vdots \\ \widetilde{\boldsymbol{T}}_3 & \ddots & \cdots & \widetilde{\boldsymbol{T}}_{\widetilde{N}+1} & \widetilde{\boldsymbol{T}}_{\widetilde{N}+2} \\ \widetilde{\boldsymbol{T}}_2 & \widetilde{\boldsymbol{T}}_3 & \cdots & \widetilde{\boldsymbol{T}}_{\widetilde{N}} & \widetilde{\boldsymbol{T}}_{\widetilde{N}+1} \end{bmatrix},\ \mathbb{T}_{23}=\begin{bmatrix} \widetilde{\boldsymbol{T}}_0 & \widetilde{\boldsymbol{T}}_1 & \cdots & \widetilde{\boldsymbol{T}}_{\widetilde{N}-2} & \widetilde{\boldsymbol{T}}_{\widetilde{N}-1} \\ \widetilde{\boldsymbol{T}}_1 & \widetilde{\boldsymbol{T}}_0 & \cdots & \ddots & \widetilde{\boldsymbol{T}}_{\widetilde{N}-2} \\ \vdots & \ddots & \ddots & \ddots & \vdots \\ \widetilde{\boldsymbol{T}}_{\widetilde{N}-2} & \ddots & \cdots & \widetilde{\boldsymbol{T}}_0 & \widetilde{\boldsymbol{T}}_1 \\ \widetilde{\boldsymbol{T}}_{\widetilde{N}-1} & \widetilde{\boldsymbol{T}}_{\widetilde{N}-2} & \cdots & \widetilde{\boldsymbol{T}}_1 & \widetilde{\boldsymbol{T}}_0 \end{bmatrix},$$

with each block $\boldsymbol{T}_k$ (given by (2.11)) and $\widetilde{\boldsymbol{T}}_k$ being $\widetilde{M}$-by-$\widetilde{M}$ Toeplitz matrix, and

$$\widetilde{\boldsymbol{T}}_k=\begin{bmatrix} t^k_{\widetilde{M}+1} & t^k_{\widetilde{M}+2} & \cdots & t^k_{2\widetilde{M}-1} & t^k_{2\widetilde{M}} \\ t^k_{\widetilde{M}} & t^k_{\widetilde{M}+1} & \ddots & \ddots & t^k_{2\widetilde{M}-1} \\ \vdots & \ddots & \ddots & \ddots & \vdots \\ t^k_3 & \ddots & \ddots & t^k_{\widetilde{M}+1} & t^k_{\widetilde{M}+2} \\ t^k_2 & t^k_3 & \cdots & t^k_{\widetilde{M}} & t^k_{\widetilde{M}+1} \end{bmatrix}. \tag{E.23}$$

The entires of $\widetilde{N}$-by-1 block-Toeplitz matrix $\mathbb{T}_{i4}$, $i=1,2,3$ are given by

$$\mathbb{T}_{14}=\begin{bmatrix} \boldsymbol{T}_{\widetilde{N}} \\ \boldsymbol{T}_{\widetilde{N}-1} \\ \vdots \\ \boldsymbol{T}_1 \end{bmatrix},\ \mathbb{T}_{24}=\begin{bmatrix} \boldsymbol{T}_1 \\ \boldsymbol{T}_2 \\ \vdots \\ \boldsymbol{T}_{\widetilde{N}} \end{bmatrix},\ \mathbb{T}_{34}=\begin{bmatrix} \widetilde{\boldsymbol{T}}^t_1 \\ \widetilde{\boldsymbol{T}}^t_2 \\ \vdots \\ \widetilde{\boldsymbol{T}}^t_{\widetilde{N}} \end{bmatrix}.$$

For the part without Toeplitz-structure $\widehat{\boldsymbol{S}}$, we denote the $\widetilde{M}$-by-2$\widetilde{M}$ matrix

$$\widetilde{\boldsymbol{D}} = [\boldsymbol{D}_{\leftarrow}^{(-1)}, \boldsymbol{D}^{(0)}] \text{ with } \boldsymbol{D}^{(n)} = \begin{bmatrix} t_{\widetilde{M}}^{n+1} & t_{\widetilde{M}}^{n+2} & \cdots & t_{\widetilde{M}}^{\widetilde{M}+n} \\ t_{\widetilde{M}-1}^{n+1} & t_{\widetilde{M}-1}^{n+2} & \ddots & t_{\widetilde{M}-1}^{\widetilde{M}+n} \\ \vdots & \ddots & \ddots & \vdots \\ t_1^{n+1} & t_1^{n+2} & \cdots & t_1^{\widetilde{M}+n} \end{bmatrix},$$

where $\boldsymbol{D}_{\leftarrow}$ denotes the matrix obtained from $\boldsymbol{D}$ by flipping each column of $\boldsymbol{D}$ in the left-right direction. Then, the entries of $\mathbb{D}_{i5}$ $i = 1,2,3,4$ are given by

$$\mathbb{D}_{15} = \begin{bmatrix} \boldsymbol{D}^{(\widetilde{M})} \\ \boldsymbol{D}^{(\widetilde{M}-1)} \\ \vdots \\ \boldsymbol{D}^{(1)} \end{bmatrix}, \mathbb{D}_{25} = \begin{bmatrix} \widetilde{\boldsymbol{D}}(\widetilde{M}) \\ \widetilde{\boldsymbol{D}}(\widetilde{M}-1) \\ \vdots \\ \widetilde{\boldsymbol{D}}(1) \end{bmatrix}, \mathbb{D}_{35} = \begin{bmatrix} \widetilde{\boldsymbol{D}}_{\uparrow}(\widetilde{M}) \\ \widetilde{\boldsymbol{D}}_{\uparrow}(\widetilde{M}-1) \\ \vdots \\ \widetilde{\boldsymbol{D}}_{\uparrow}(1) \end{bmatrix}, \mathbb{D}_{45} = \widetilde{\boldsymbol{D}}(\widetilde{M}+1).$$

where the $\widetilde{M}$-by-$\widetilde{M}$ matrix $\widetilde{\boldsymbol{D}}(n) = \widetilde{\boldsymbol{D}}(:, n : n+\widetilde{M}-1)$, and $\widetilde{\boldsymbol{D}}_{\uparrow}(n)$ denote each row of $\widetilde{\boldsymbol{D}}(n)$ is flipped in the up-down direction.

Acknowledgments

The research of first author is partially supported by the National Natural Science Foundation of China (Nos. 12201385 and 12271365), Shanghai Pujiang Program 21PJ1403500, the Fundamental Research Funds for the Central Universities 2021110474 and Shanghai Post-doctoral Excellence Program 2021154. The research of second author is partially supported by Singapore MOE AcRF Tier 1 Grant: RG15/21. The research of the third author is partially supported by the Natural Science Foundation of Hunan Province (No. 2022JJ30996). The work of fourth author is partially supported by the National Natural Science Foundation of China (No. 11871455 and 11971016).

This work was done partially while the author was participating in the program of the Institute for Mathematical Sciences, National University of Singapore, in 2022.

Conflict of interest

The authors declare that they have no conflict of interest.

References

[1] Multiprecision Computing Toolbox, Advanpix, Tokyo. *http://www.advanpix.com*.

[2] G. Acosta and F. M. Bersetche. Numerical approximations for a fully fractional Allen-Cahn equation. *ESAIM Math. Model. Numer. Anal.*, 55:S3–S28, 2021.

[3] G. Acosta, F. M. Bersetche, and J. P. Borthagaray. A short FE implementation for a 2d homogeneous Dirichlet problem of a fractional Laplacian. *Comput. Math. Appl.*, 74(4):784–816, 2017.
[4] G. Acosta and J. P. Borthagaray. A fractional Laplace equation: regularity of solutions and finite element approximations. *SIAM J. Numer. Anal.*, 55(2):472–495, 2017.
[5] M. Ainsworth and C. Glusa. Aspects of an adaptive finite element method for the fractional Laplacian: a priori and a posteriori error estimates, efficient implementation and multigrid solver. *Comput. Methods Appl. Mech. Engrg.*, 327:4–35, 2017.
[6] M. Ainsworth and C. Glusa. Towards an efficient finite element method for the integral fractional Laplacian on polygonal domains. In *Contemporary computational mathematics—a celebration of the 80th birthday of Ian Sloan. Vol. 1, 2*, pages 17–57. Springer, Cham, 2018.
[7] H. Antil, P. Dondl, and L. Striet. Approximation of integral fractional Laplacian and fractional PDEs via sinc-basis. *SIAM J. Sci. Comput.*, 43(4):A2897–A2922, 2021.
[8] A. Bonito, J. P. Borthagaray, R. H. Nochetto, E. Otárola, and A. J. Salgado. Numerical methods for fractional diffusion. *Comput. Vis. Sci.*, 19(5-6):19–46, 2018.
[9] A. Bonito, W. Lei, and J. E Pasciak. Numerical approximation of the integral fractional Laplacian. *Numer. Math.*, 142(2):235–278, 2019.
[10] J. P. Borthagaray and J. P. Ciarlet. On the convergence in H^1-norm for the fractional Laplacian. *SIAM J. Numer. Anal.*, 57(4):1723–1743, 2019.
[11] J. P. Borthagaray, L. M Del Pezzo, and S. Martinez. Finite element approximation for the fractional eigenvalue problem. *J. Sci. Comput.*, 77(1):308–329, 2018.
[12] J. P. Borthagaray, D. Leykekhman, and R. H. Nochetto. Local energy estimates for the fractional Laplacian. *SIAM J. Numer. Anal.*, 59(4):1918–1947, 2021.
[13] J. P. Borthagaray and R. H. Nochetto. Besov regularity for the Dirichlet integral fractional Laplacian in Lipschitz domains. *J. Funct. Anal.*, 284(6):Paper No. 109829, 33, 2023.
[14] W. Boukaram, M. Lucchesi, G. Turkiyyah, O. Le Maitre, O. Knio, and D. Keyes. Hierarchical matrix approximations for space-fractional diffusion equations. *Comput. Methods Appl. Mech. Eng.*, 369:113191, 2020.
[15] J. Burkardt, Y. Wu, and Y. Zhang. A unified meshfree pseudospectral method for solving both classical and fractional PDEs. *SIAM J. Sci. Comput.*, 43(2):A1389–A1411, 2021.
[16] K. Burrage, N. Hale, and D. Kay. An efficient implicit FEM scheme for fractional-in-space reaction-diffusion equations. *SIAM J. Sci. Comput.*, 34(4):A2145–A2172, 2012.
[17] R. H. Chan and X. Jin. *An introduction to iterative Toeplitz solvers*, volume 5. SIAM, 2007.
[18] H. Chen, C. Sheng, and L.-L. Wang. On explicit form of the FEM stiffness matrix for the integral fractional Laplacian on non-uniform meshes. *Appl. Math. Lett.*, 113:106864, 2021.
[19] W. Chen, Y. Li, and P. Ma. *The Fractional Laplacian*. World Scientific, 2020.
[20] M. D'Elia, Q. Du, C. Glusa, M. Gunzburger, X. Tian, and Z. Zhou. Numerical methods for nonlocal and fractional models. *Acta Numer.*, 29:1–124, 2020.
[21] Q. Du. *Nonlocal modeling, analysis, and computation*, volume 94 of *CBMS-NSF Regional Conference Series in Applied Mathematics*. Society for Industrial and Applied Mathematics (SIAM), Philadelphia, PA, 2019.
[22] S. Duo, H. W. van Wyk, and Y. Zhang. A novel and accurate finite difference method for the fractional Laplacian and the fractional poisson problem. *J. Comput. Phys.*, 355:233–252, 2018.
[23] S. Duo and Y. Zhang. Computing the ground and first excited states of the fractional schrödinger equation in an infinite potential well. *Commun. Comput. Phys.*, 18(2):321–350, 2015.
[24] S. Duo and Y. Zhang. Accurate numerical methods for two and three dimensional integral

fractional Laplacian with applications. *Comput. Methods Appl. Mech. Eng.*, 355:639–662, 2019.

[25] M. Faustmann, M. Karkulik, and J. M. Melenk. Local convergence of the FEM for the integral fractional Laplacian. *SIAM J. Numer. Anal.*, 60(3):1055–1082, 2022.

[26] I. S. Gradshteyn and I. M. Ryzhik. *Table of Integrals, Series, and Products*. Elsevier/Academic Press, Amsterdam, eighth edition, 2015. Translated from the Russian, Translation edited and with a preface by Daniel Zwillinger and Victor Moll, Revised from the seventh edition [MR2360010].

[27] G. Grubb. Fractional Laplacians on domains, a development of Hörmander's theory of μ-transmission pseudodifferential operators. *Adv. Math.*, 268:478–528, 2015.

[28] Z. Hao, Z. Zhang, and R. Du. Fractional centered difference scheme for high-dimensional integral fractional Laplacian. *J. Comput. Phys.*, 424:109851, 2021.

[29] M. Karkulik and J. M. Melenk. $\mathcal{H}$-matrix approximability of inverses of discretizations of the fractional Laplacian. *Adv. Comput. Math.*, 45(5):2893–2919, 2019.

[30] D. Li, C. Quan, and T. Tang. Stability and convergence analysis for the implicit-explicit method to the Cahn-Hilliard equation. *Math. Comp.*, 91(334):785–809, 2022.

[31] A. Lischke, G. Pang, M. Gulian, and et al. What is the fractional Laplacian? A comparative review with new results. *J. Comput. Phys.*, 404:109009, 2020.

[32] H. Liu, C. Sheng, L.-L. Wang, and H. Yuan. On diagonal dominance of FEM stiffness matrix of fractional Laplacian and maximum principle preserving schemes for fractional Allen-Cahn equation. *J. Sci. Comput.*, 86(2):1–28, 2021.

[33] W. McLean. *Strongly Elliptic Systems and Boundary Integral Equations*. Cambridge University Press, Cambridge, 2000.

[34] V. Minden and L. Ying. A simple solver for the fractional Laplacian in multiple dimensions. *SIAM J. Sci. Comput.*, 42(2):A878–A900, 2020.

[35] E. Di Nezza, G. Palatucci, and E. Valdinoci. Hitchhiker's guide to the fractional Sobolev spaces. *Bull. Sci. Math.*, 136:521–573, 2012.

[36] F.W.J. Olver, D.W. Lozier, R.F. Boisvert, and C.W. Clark, editors. *NIST Handbook of Mathematical Functions*. U.S. Department of Commerce, Cambridge University Press, Cambridge, 2010.

[37] C. Sheng, D. Cao, and J. Shen. Efficient spectral methods for PDEs with spectral fractional Laplacian. *J. Sci. Comput.*, 88(1):1–26, 2021.

[38] C. Sheng, J. Shen, T. Tang, L.-L. Wang, and H. Yuan. Fast Fourier-like mapped Chebyshev spectral-Galerkin methods for PDEs with integral fractional Laplacian in unbounded domains. *SIAM J. Numer. Anal.*, 58(5):2435–2464, 2020.

[39] F. Song, C. Xu, and G. E. Karniadakis. A fractional phase-field model for two-phase flows with tunable sharpness: Algorithms and simulations. *Comput. Methods Appl. Mech. Engrg.*, 305:376–404, 2016.

[40] T. Tang, L. Wang, H. Yuan, and T. Zhou. Rational spectral methods for PDEs involving fractional Laplacian in unbounded domains. *SIAM J. Sci. Comput.*, 42(2):A585–A611, 2020.

[41] T. Tang, H. Yuan, and T. Zhou. Hermite spectral collocation methods for fractional PDEs in unbounded domains. *Commun. Comput. Phys.*, 24(4):1143–1168, 2018.

[42] C. Vollmann and V. Schulz. Exploiting multilevel Toeplitz structures in high dimensional nonlocal diffusion. *Comput. Vis. Sci.*, 20(1-2):29–46, 2019.

[43] H. Wang and T. S. Basu. A fast finite difference method for two-dimensional space-fractional diffusion equations. *SIAM J. Sci. Comput.*, 34(5):A2444–A2458, 2012.